AWARD NUMBER: W81XWH-16-1-0017

TITLE: A 3D Bioprinted Model for the Study of Premalignant Disease

PRINCIPAL INVESTIGATOR: Adrian V. Lee, PhD

CONTRACTING ORGANIZATION: University of Pittsburgh

REPORT DATE: Aug 2019

TYPE OF REPORT: Final

PREPARED FOR: U.S. Army Medical Research and Materiel Command

Fort Detrick, Maryland 21702-5012

REPORT DOCUMENTATION PAGE

Form Approved
OMB No. 0704-0188

1. REPORT DATE	2. REPORT TYPE	3. DATES COVERED
August 2019	Final	05/01/2016 - 04/30/2019

4. TITLE AND SUBTITLE

A 3D Bioprinted Model for the Study of Premalignant Disease

5a. CONTRACT NUMBER

5b. GRANT NUMBER
W81XWH-16-1-0017

5c. PROGRAM ELEMENT NUMBER

6. AUTHOR(S)

Adrian V. Lee, PhD

5d. PROJECT NUMBER

5e. TASK NUMBER

5f. WORK UNIT NUMBER

7. PERFORMING ORGANIZATION NAME(S) AND ADDRESS(ES)

University of Pittsburgh
4200 Fifth Ave,
Pittsburgh,
PA 15260

8. PERFORMING ORGANIZATION REPORT NUMBER

9. SPONSORING / MONITORING AGENCY NAME(S) AND ADDRESS(ES)

U.S. Army Medical Research and Materiel Command
Fort Detrick, Maryland 21702-5012

10. SPONSOR/MONITOR'S ACRONYM(S)

11. SPONSOR/MONITOR'S REPORT NUMBER(S)

12. DISTRIBUTION / AVAILABILITY STATEMENT

Approved for Public Release; Distribution Unlimited

13. SUPPLEMENTARY NOTES

14. ABSTRACT

This proposal involved a multidisciplinary team including a surgical oncologist, a mammary gland biologist, a biomedical engineer, and a cancer biologist. We hypothesized that a novel in vitro 3D bioprinted model of premalignant breast cells growing within a breast ductal system will represent a faithful representation of premalignant progression *in vitro* and will be an outstanding model for identify markers of low-risk premalignant disease which doesn't require treatment**.** To build the model, we first quantified murine mammary gland development, finding strain dependent differences highlighting a genetic component. We developed a proof-of-principle 3D printing technology to print a mammary gland, and comprehensively developed a 3D printed ductal system with perfusion to study breast cells in their 3D environment. We have iteratively improved the quality and fidelity of the 3D printed ductal system composed of collagen and other ECM proteins and examined growth and behavior of breast cells in this 3D mammary duct in vitro. Further development of this model may help in understanding premalignant forms of breast cancer.

15. SUBJECT TERMS

16. SECURITY CLASSIFICATION OF:			17. LIMITATION OF ABSTRACT	18. NUMBER OF PAGES	19a. NAME OF RESPONSIBLE PERSON
a. REPORT	b. ABSTRACT	c. THIS PAGE			19b. TELEPHONE NUMBER *(include area code)*
Unclassified	Unclassified	Unclassified	Unclassified		USAMRMC

Standard Form 298 (Rev. 8-98)
Prescribed by ANSI Std. Z39.18

Table of Contents

1) Introduction……4

2) Keywords……4

3) Accomplishments……4

4) Impact……..34

5) Changes/problems……34

6) Products……35

7) Participants and other collaborating organizations……..35

8) Special reporting requirements……35

9) Appendices……...35

1) Introduction

This proposal involved a multidisciplinary team including a surgical oncologist, a mammary gland biologist, a biomedical engineer, and a cancer biologist. **We hypothesized that a novel in vitro 3D bioprinted model of premalignant breast cells growing within a breast ductal system will represent the first and most faithful representation of premalignant progression *in vitro* and will be an outstanding model for identify markers of low-risk premalignant disease which doesn't require treatment.** To build the model, we first quantified murine mammary gland development, finding strain dependent differences highlighting a genetic component. We developed a proof-of-principle 3D printing technology to print a mammary gland, and comprehensively developed a 3D printed ductal system with perfusion to study breast cells in their 3D environment. We have iteratively improved the quality and fidelity of the 3D printed ductal system composed of collagen and other ECM proteins and examined growth and behavior of breast cells in this 3D mammary duct in vitro. Further development of this model may help in understanding premalignant forms of breast cancer.

2) Keywords

DCIS, ductal cancer in situ, 3D bioprinting

3) Accomplishments

Regulatory approvals

We obtained an IRB letter of exemption that the work is not human subjects research and also IACUC approval for animal work at Baylor College of Medicine. We subsequently received HRPO/ACURO approval. All approvals were renewed yearly.

Research progress

Major Task 1

Subtask 1: Purchase and breed mating pairs for 12 strains of mice from which to isolate mammary tissue wholemounts for 3D imaging from virgin females at 2 developmental ages. We purchased and bred mating pairs for 12 strains of mice from which we isolated mammary tissue wholemounts for 3D imaging from virgin females at 2 developmental ages. Of the 12 strains we were able to establish productive breeding colonies for 11. One of the 12 strains, CAST/EiJ, was difficult to obtain offspring from in high enough numbers to be useful despite the fact that we purchased additional mating pairs to compensate for reduced fecundity in this strain. This last strain was thus left out of further studies.

Subtask 2: Whole mount mammary glands (60) from PN17 mice, stain with luminal and myoepithelial markers, and capture tomography data at the OIVM core. This subtask consisted of whole mounting mammary glands (60) from post-natal day 17 (PN17) mice, stain with luminal and myoepithelial markers, and capture tomography data at the OIVM core. Examples of stained samples are shown in Figure 1.

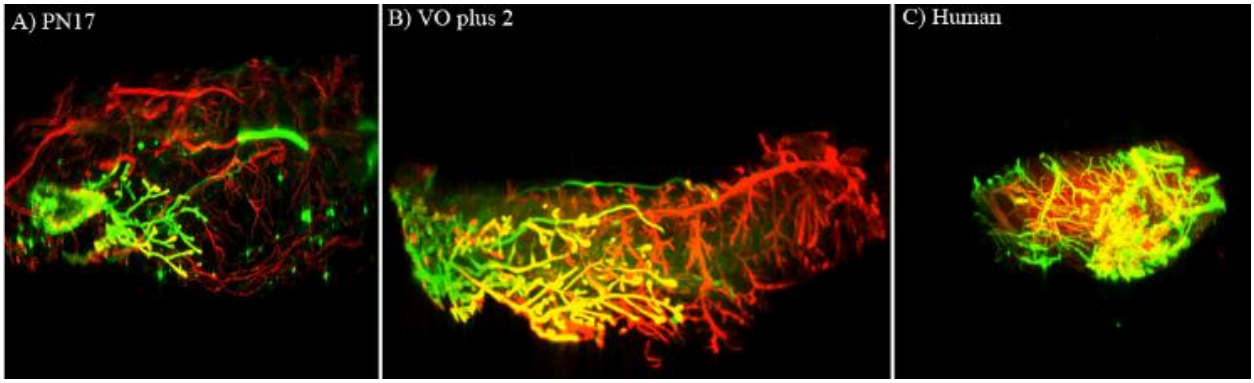

Figure 1. 3D reconstructions of Mouse and Human Mammary tissue. Mammary glands are shown from mice at post-natal day 17 (A) and 2 weeks post-vaginal opening (PN64) (B), and from a biopsy sample of normal human breast (C). Staining for E-cadherin (green) highlights the ductal epithelium. Staining for alpha-smooth muscle actin highlights blood vessels (red) and ductal myoepithelial cell layer (yellow).

This age of mouse was chosen because it represents an age just prior to the onset of puberty where the development of the gland is relatively simple and not yet under the dominating influence of estrus cycles.

Subtask 3 Segment, annotate, and measure 3D reconstructions obtained in Subtask 2. Send the annotated 3D rendering data to Pittsburg for 3D printing. This subtask consisted of segmentation, annotation, and measurement of the ductal trees in 3D reconstructions obtained in Subtask 2. 11 of 12 planned strains were analyzed for 8 of the 10 measurements that were planned. We also sent reconstruction data from PN17 samples to the University of Pittsburg/Carnegie Mellon University for 3D printing. A summary of the data from 5 of the completed strains was presented in a poster during year 1 at the 2017 Experimental Biology Meetings in Chicago IL. This work represented the first 3D comparison of ductal architecture and patterning in inbred mouse strains of different genetic backgrounds. The hypothesis for the study was that ductal patterning, and the implementation of stereotypical branching behaviors during early post-natal development differs with genetic background. A software package called TreeSurveyor (Short and coworkers, 2013) was used to identify, annotate, and measure all of the ductal segments and branch points in each reconstructed tree.

Comparisons of overall ductal geometry among the 11 completed strains revealed that genetic background had significant ($P<0.05$) effects on all but two of the traits that were measured. Figure 2 shows the effects of genetic background on overall mammary ductal geometry. Differences were evident in total duct length (Figure 2A), average duct length (Figure 2B), total branch count (Figure 2C), and branch density (Figure 2D), as well as in ductal segment diameter (Figure 2E) and curvature (Figure 2F). With regard to total ductal length (Figure 2A), there was about a 2.5-fold difference ($P<0.05$) between strains at the top (C57BL/6J, CZECHII/EiJ and PWK/PhJ) and bottom (A/J, WSB/EiJ, NOD/LtJ) ends of the distribution. This difference was primarily driven by the fact that these same strains displayed similar

differences in the average ductal segment length (Figure 2B). For some strains, such as CZECHII/EiJ, total branch count (Figure 2C) may have also contributed somewhat to overall length of the ductal tree. In this regard, there were also strains such as 129S1/SvImJ and Bub/BnJ that had high total branch counts, but short duct length, which resulted in high overall branch density (Figure 2D). Overall ductal diameter (Figure 2E) was highest in PWK/PhJ and CZECHII/EiJ, however, there were two strains, C57BL6J and KK/HlJ, that displayed high levels of intra-strain variation for this trait. Ductal curvature (Figure 1F) was highest for BUB/BnJ and WSB/EiJ, which were also strains that displayed the highest branch density overall. Neither bifurcation angle (Figure 2G) nor dihedral angle (Figure 1H) were influenced by genetic background. The overall mean for bifurcation angle was 96.9±5.0 degrees and ranged from a high of 101±5^{o} in NOD/LtJ to a low of 93±2^{o} in PWK/PhJ suggesting the in general bifurcation events during branching morphogenesis tend to be right angles. For dihedral angle the overall mean was 76.5±6.9 degrees with a high of 79±3^{o} in NOD/LtJ and a low of 74±3 in KK/HlJ implying that in general branching events during ductal morphogenesis in the mammary gland are orthogonal with respect to rotation.

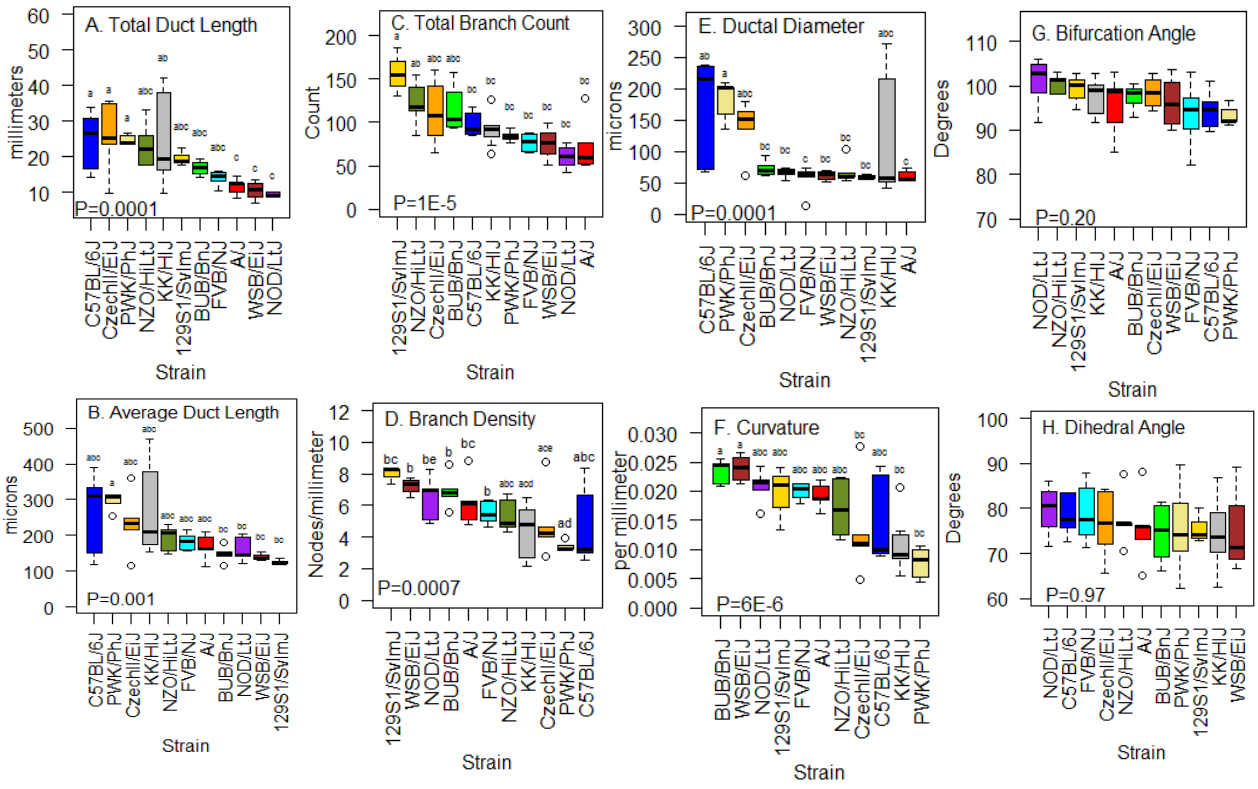

Figure 2. Genetic Background influences overall mammary ductal geometry. Three-dimensional reconstructions were prepared from E-cadherin-stained mammary whole mounts. Tissues were collected from females of 11 different inbred strains at post-natal day 17 of age. Shown are (A) total duct length, (B) average duct length, (C) total branch count, (D) branch density, (E) ductal diameter, (F) curvature, (G) bifurcation angle, and (H) dihedral angle. Each box represents the data for 3 to 7 animals. Statistical significance was set at α=0.05. Boxes are ordered by strain median. Boxes with similar superscripts are similar (P>0.05) by Tukey's HSD.

Analysis of regional variation within the ductal trees at PN17 was also accomplished in all 11 strains. The results of this regional analysis are shown in Figure 3. A significant effect of generation was detected for branch count (Figure 3A), length (Figure 3B) diameter (Figure 3C), and curvature (Figure 3D). For branch count (Figure 3A), all 11 strains exhibited a continuous increase for at least the first 6 generations. However, by generation 5 the strains started to differentiate themselves. For some, like NZO/LtJ and 129S1SvImJ, branch counts continued to increase through the next 5 to 7 generations and then dropped off in later generations. Others like NOD/LtJ, WSB/EiJ and A/J, added branches at a slower rate. For all 11 strains average duct length (Figure 3B) was highest in the root (generation 0) and first-generation branches and decreased with branch generation. The exception observed in branch length was with KK/HlJ, which appeared to have increase in branch length in later generation. This increase, however, was only observed in a single animal. Branch diameter (Figure 3C) similarly started out highest in the early generations and gradually decreased with progression toward later generations. In this regard there were 4 strains C57BL/6J, PWK/PhJ, CZECHII/EiJ, and KK/HlJ that exhibited much larger branch diameters than the remaining strains. Differences were also observed in branch curvature among certain strains with progression through ductal tree (Figure 3D). In

general, among the strains that exhibited generation-dependent variation, curvature tended to be highest in earlier generations. Neither bifurcation angle (Figure 3E) nor dihedral angle (Figure 3F) changed significantly with generation. In this regard, an inability to observe changes could possibly be attributed to the fact that both internal and terminal branches both contribute to these two measurements. We are currently in the process of classifying the branches based on their relative location within the ductal tree. The TreeSurveyor package has an option that will allow for stratification of individual branches on the basis of whether they are internal or terminal. This should allow us to determine with greater selectively, if branch angles and even the other traits discussed are affected by whether they are internal or terminal structures. These results support the preliminary conclusion that genetic background, acting through sequence variants at specific genomic loci, can influence ductal diameter, length, and curvature.

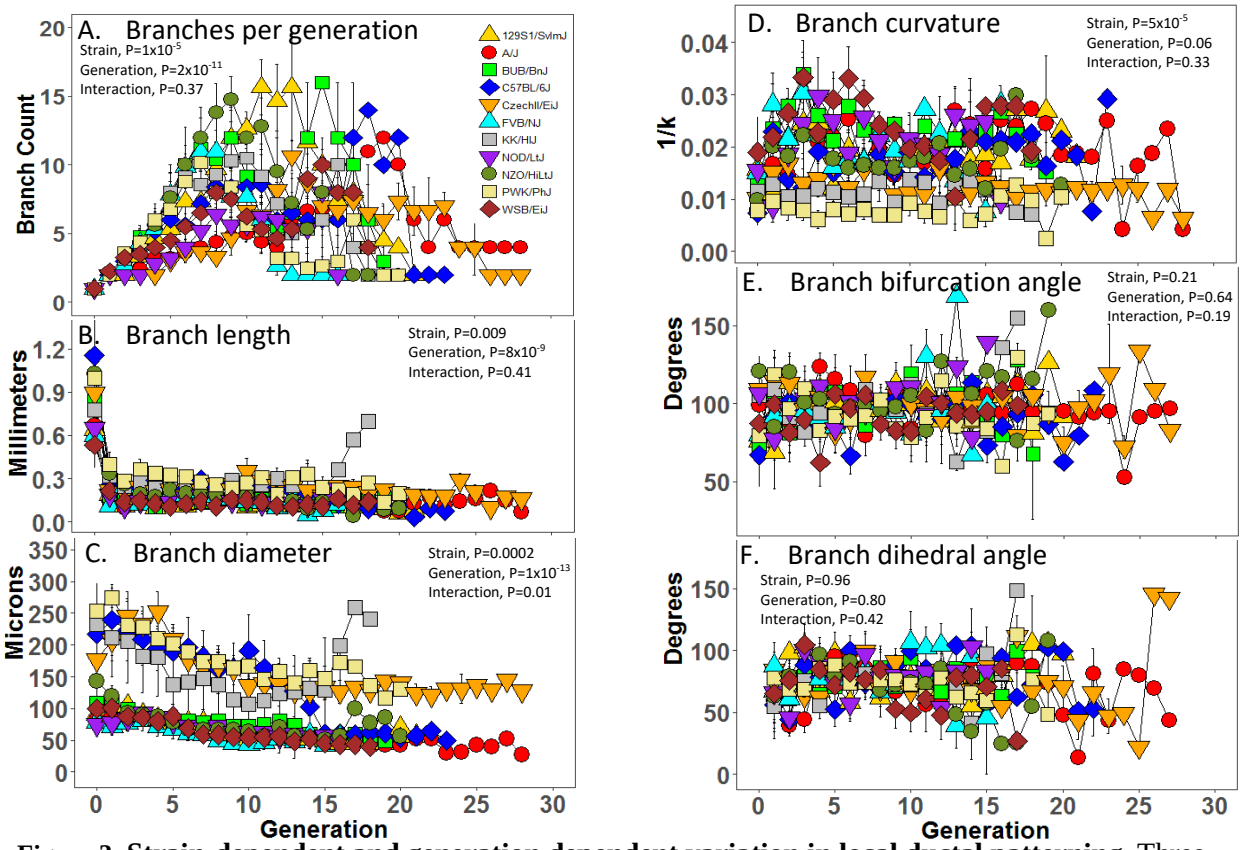

Figure 3. Strain-dependent and generation dependent variation in local ductal patterning. Three-dimensional reconstructions were prepared from E-cadherin-stained mammary wholemounts. Tissues were collected from females of 11 different inbred strains at post-natal day 17 of age. Shown are (A) branch count, (B) branch length, (C) branch segment diameter, (D) branch curvature, (E) bifurcation angle, and (F) dihedral angle. Each symbol represents the mean±s.e.m. for 3 to 7 animals. Statistical significance was set at α=0.05.

Subtask 4 Whole mount mammary glands from PN64 mice, stain with luminal and myoepithelial markers, and capture tomography data at the SANTA core.

This sub-task involved whole mount staining mammary glands (60) from PN64 mice for the same luminal and myoepithelial markers used on the PN17 mice. We collected at least 1 sample from all but two of the proposed strains (Table 1). In addition, during the course of identifying prospective mice for sampling, all of the females within the breeding colonies for the 11 strains studied were observed for the timing of sexual maturation, as indicated by vaginal patency. The results of this analysis are shown in figure 4. Genetic background has a dramatic effect ($P=2x10^{-16}$) on the timing of sexual maturation. This fact is a very important consideration to the interpretation of data from the PN64 samples. In particular, wild-derived strains such as CZECHII/EiJ, PWK/PhJ, and WSB/EiJ can undergo sexual maturation up to two weeks later that some of the classical strains such as BUB/BnJ. However, although samples from some of the strains were successfully stained and imaged at PN64, a majority of the samples that we tried to stain did not provided useful reconstructions because of a lack of specific signal within the center of the specimens. An example of this is shown in Figure

Table 1. Progress on PN64 sample processing

STRAIN	Usable samples processed
129S1	5
A/J	1
BUB/BnJ	0
C57BL6/J	5+
CAST/EiJ	0
CZECHII/EiJ	3
FVB/NJ	2
KK/HlJ	5+
NOD/ShILtJ	1
NZO/HltJ	0
PWK/PhJ	2
WSB/EiJ	2

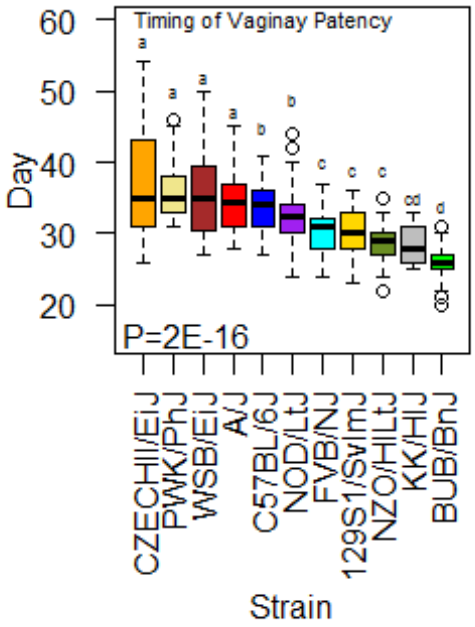

Figure 4. Timing of Vaginal Patency. Vaginal patency was detected visually in cohorts of prospective study females beginning with weaning at post-natal day 21. Each bar represents the data for from 20 to 122 females that were visually observed twice weekly until observation of vaginal opening. Bars with similar superscripts are similar (P>0.05) by Tukey's HSD.

5. In dealing with this issue we attempted a variety of approaches to increase the signal include varying the amount and type of detergents used to solubilize the tissue, varying the time of fixative exposure and retesting the dilutions of the antibodies used in the staining. None of these produced useable specimens. As a consequence, the decision was made to obtain ancillary data concerning other processes that could be linked to variations in the patterning of the ductal tree from PN17 females. Concentrations of estradiol (Figure 6B) and progesterone (Figure 6C) were measured in urine samples collected from females from each of 13 strains at weaning on PN21. Urinary creatinine (Figure 6A) was used to correct for variation due to hydration. All three analytes were affected ($P<0.05$) by genetic background. Average estradiol concentrations ranged from a low of 2.3±0.6 ng/mg creatinine in WSB/EiJ to a high of 6.9±1.5 ng/mg in PL/J. Progesterone concentration was also lowest in WSB/EiJ (19.1±8.7). The strains with the highest

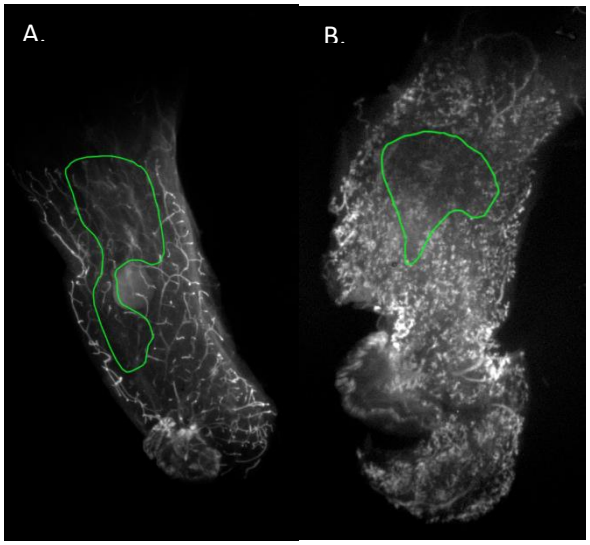

Figure 5. Incomplete staining of larger PN64 samples. Panel A. is from a PN64 NOD/LtJ. Panel B is from a PN64 BUB/BnJ.

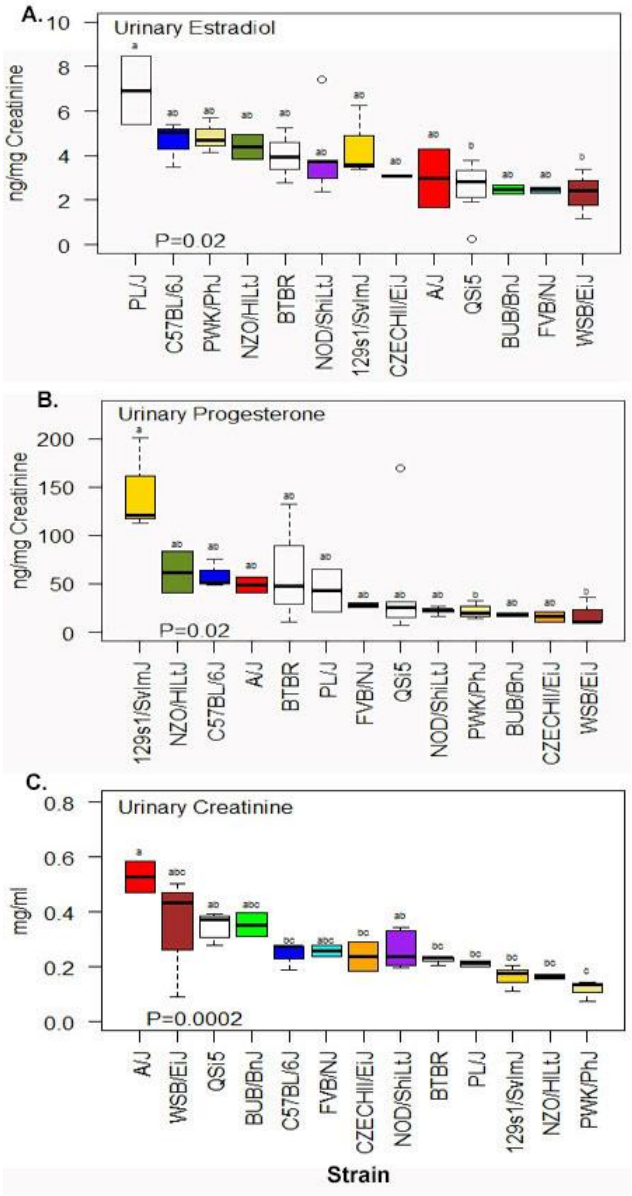

Figure 6. Urinary estrogen and progesterone pre-weaning females is affected by genetic background. Urine samples were collected from weaning age females at PN21. Estrogen (A) and Progesterone (B) was measured by ELISA. Creatinine (C) was measured using a colorimetric assay and used to adjust the steroid concentrations for difference in hydrations. Each box represents the data from 2 - 8 animals. Boxes with similar superscripts are similar ($P>0.05$) by Tukey's HSD.

urinary progesterone was 129s1/SvImJ (144.8±28.1 ng/mg creatinine). This concentration averaged 4-fold more that the average of all the remaining strains combined. This result suggested that in 129s1/SvImJ there are a unique combination of biological factors that lead elevated systemic level of progesterone in comparison to other inbred strains.

To determine if the observed strain dependent variation in estrogen and progesterone were correlated with variations in sexual maturation or ductal patterning in the PN17 mammary ductal tree, strain means were used in a correlation analysis. The lattice plot (Figure 7) displays scatter plots, histograms, and Pearson's correlations relating all of the features in the dataset. Significant

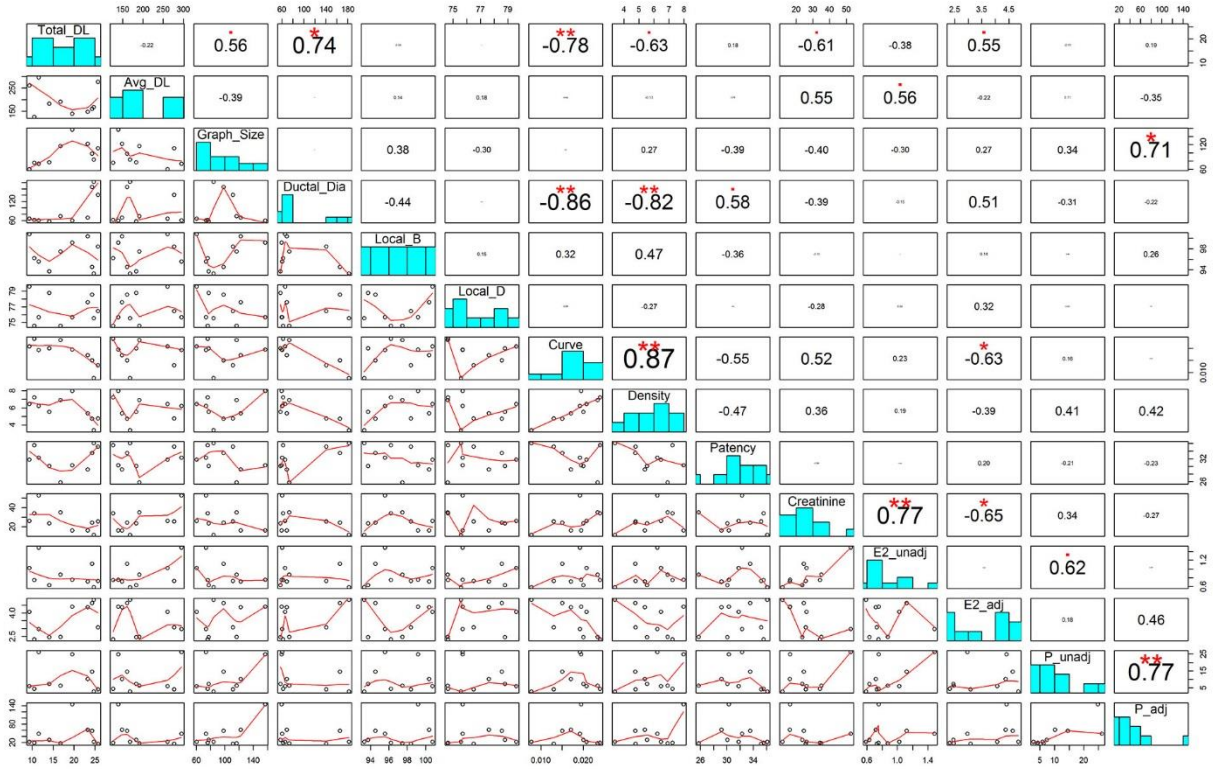

Figure 7. Correlations among urinary steroids, sexual maturation, and mammary ductal geometry. Concentrations of estradiol, progesterone, and creatinine were measured in urine samples collected from PN21 females of 13 different inbred mouse strains and compared with the onset of sexual maturation, as measured by vaginal patency, and with 8 pre-weaning mammary ductal geometry traits. Scatter plots are presented in the lower left of the lattice, histograms are presented on the diagonal, and Pearson's r is presented on the upper right of the lattice Ductal development traits were presented by strain in figure 1 and include total duct length (Total_DL), average duct length (AVG_DL), total number of branch nodes (Graph_size), median ductal diameter (Ductal_Dia), Local bifurcation angle (Local_B), local dihedral angle (Local_D), ductal curvature (Curve), and branch density (Density). Sexual maturation (Patency) is from figure 3. Absolute concentrations of estradiol (E2_unadj) and progesterone (P_unadj) were determined by ELISA and adjusted for hydration level using urinary creatinine (Figure 4). Correlations coefficients with exceedingly small font sizes are close to zero. Each symbol is a strain mean obtained. Red asterisks, indicate statistical significance (***P<0.001, **P<0.01, *P<0.05, ■P<0.10).

(P<0.05) Pearson's correlations were observed among 9 of the 91 possible comparisons that were made. Among the ductal traits, branch density was positively correlated with branch curvature (r=0.87), negatively correlated with ductal diameter (r=-0.86) and negatively correlated with total duct length (r=-0.78). Ductal curvature was also negatively correlated with both ductal diameter (r=-.86), and total duct length (-0.78), while ductal diameter was positively correlated (r=0.74) with total duct length. With regard to the urinary analytes, creatinine was positively correlated (r=0.77) with the unadjusted concentration of estradiol and negatively correlated (r=-0.65) with the creatinine-adjusted estradiol concentration (E2adj). Creatinine adjusted estradiol was negatively correlated (r=-0.63) with ductal curvature (Figure 8A), and positively correlated (r=0.55) with total duct length (Figure 8B). Urinary progesterone was positively correlated (r=0.77) with creatinine-adjusted urinary progesterone (Figure 8), and creatinine-adjusted urinary progesterone was highly correlated (r=0.77) with graph size (Figure 8C). These results support

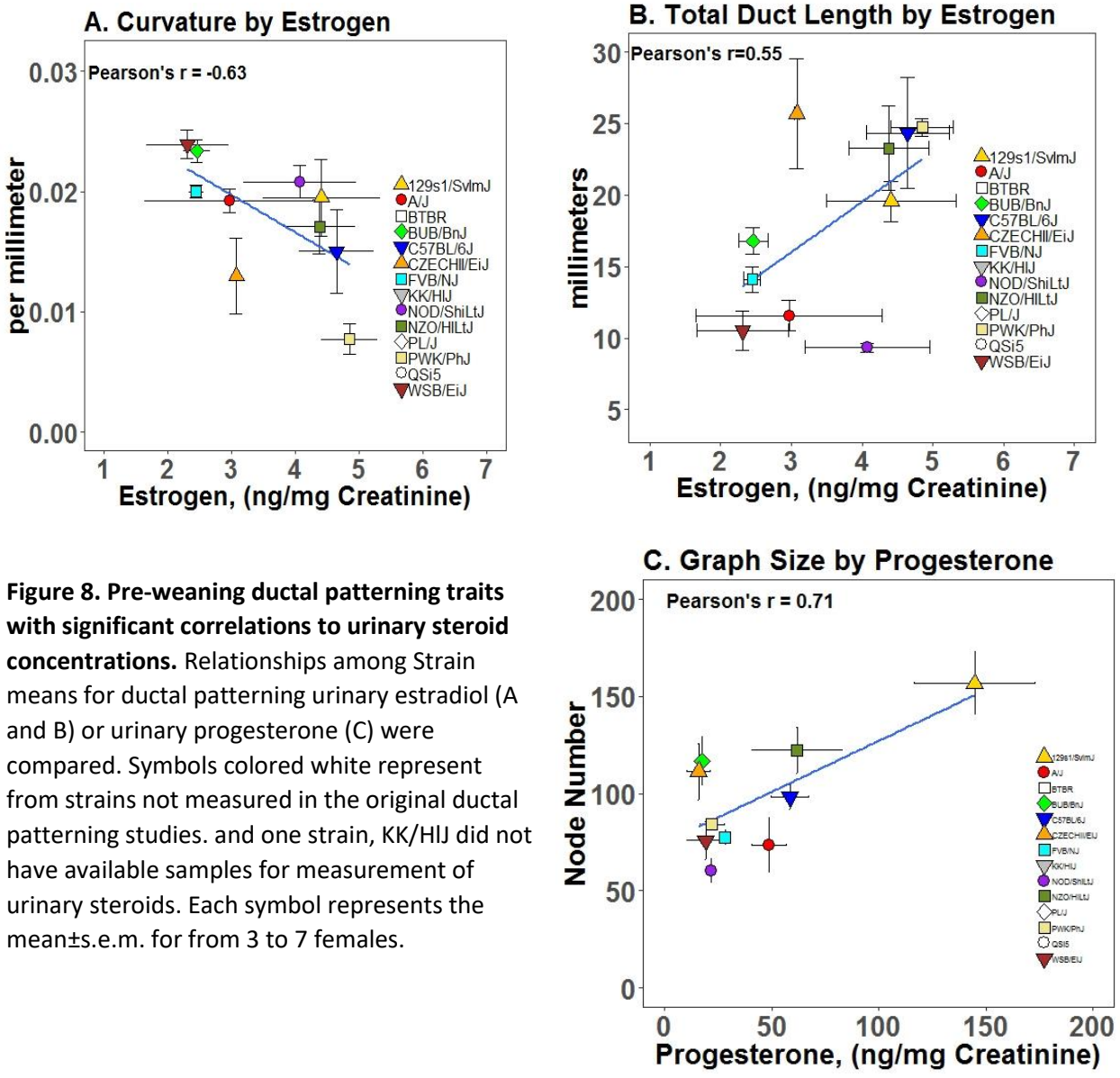

Figure 8. Pre-weaning ductal patterning traits with significant correlations to urinary steroid concentrations. Relationships among Strain means for ductal patterning urinary estradiol (A and B) or urinary progesterone (C) were compared. Symbols colored white represent from strains not measured in the original ductal patterning studies. and one strain, KK/HlJ did not have available samples for measurement of urinary steroids. Each symbol represents the mean±s.e.m. for from 3 to 7 females.

the conclusion genetic background affects mammary ductal development and pattering in pre-pubertal, pre-weaning, females of through effects mediated by circulating estrogen and progesterone. These results will be incorporated into a manuscript describing the effects of genetic background on mammary ductal development and pattering in pre-weaning female mice.

Subtask 5: Purchase lactating dams with litters (2 each) for each of 3 rat strains. The strains will be ACI/Seg/Hsd from Harlan Laboratories, and Sprague-Dawley and Wistar, both from Charles River Laboratories. There will be 5 females studied at PN64 for each of the 3 strains. This sub-task was not completed due to size limitations in the imaging instruments and an inability to get enzyme-metallography to work.

Subtask 6: Whole mount mammary glands (15) from PN64 rats, stain with luminal and myoepithelial markers, and capture tomography and Micro-CT data at the OIVM core. After several attempts at staining these larger samples for enzyme metallography we concluded that this subtask was infeasible.

Major Task 2

Task 2 Subtask 1 was to 3D print mammary ductal structure images using ECM hydrogels. was to be completed during months 4 through 12 and was to 3D print mammary ductal structure images using ECM hydrogels. This subtask has been completed and we have fully developed and implemented this capability. To do this we needed to implement a new 3D bioprinting approach that allowed us to directly print with collagen type I and additional ECM protein hydrogels while achieving high fidelity and resolution better than 100 μm.

First, we needed to develop a process to print multiple materials, in order to have a temporary support material that would provide mechanical strength and enable handling of the delicate mammary ductal structures, which consist of small diameter tubes that branch in 3D space. A collagen hydrogel containing cells will often compact over time due to the adhesion, proliferation, and remodeling of the cells. If this process is unregulated, many constructs will compact to a dense state containing a necrotic core. Many engineered tissues consist of a cellular gel that is compacted around a mandrel or series of rigid posts meant to align internal cells based on the stresses inside the gel. In an unconstrained tubular construct, compaction would manifest as initial closure of the internal lumen and eventual fusion into a dense mass. It is therefore reasonable to expect an engineered branching construct such as a ductal epithelium to compact into a denser, dysfunctional state with necrotic regions and partial lumen closure. While it may be possible to formulate a collagenous, cellular hydrogel ink that does not compact in culture, the requirements for this are likely beyond the scope of this project. Instead, it should be easier to embed the collagen construct inside a sparse net of rigid alginate hydrogel extrusions (Figure 9A). Forces that normally deform the collagen hydrogel would instead be forced to work against the alginate mesh that surrounds the construct. The alginate would be included in the print as a separate ink in an additional extruder, and the mesh would be generated as a sparse infill pattern normally seen in the interior of 3D prints. Testing this approach of immobilizing one printed material within another would likely require a simplified geometry such as a vertical tube of collagen gel to be printed in alginate mesh (Figure 9C). Measuring the dimensions of the tube is

accomplished as with the gauging of print accuracy using calibration prints – micrographs are compared with known digital dimensions. By using this approach, we can fabricate a cellular collagenous tube coated in epithelium and maintain its geometry while in culture, making it possible to then create a complete epithelial tree.

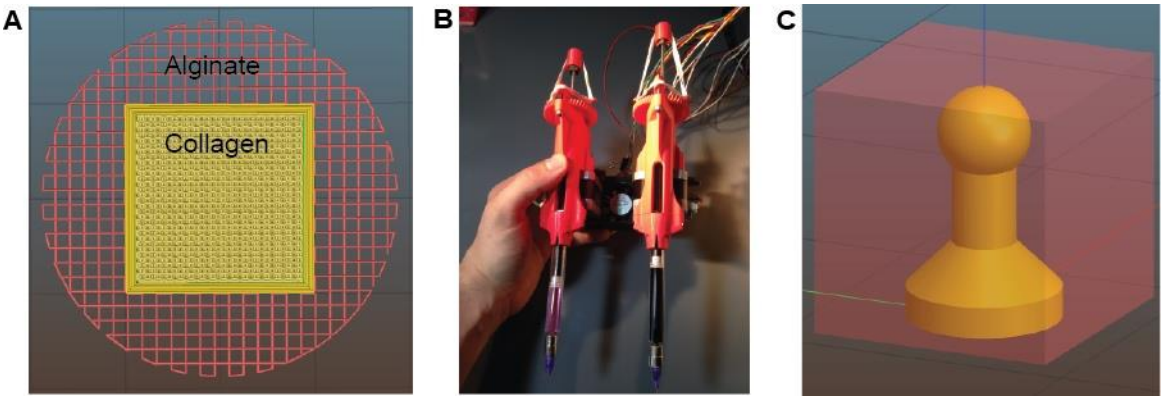

Figure 9. Utilizing Dual Extrusion to Reinforce Soft Hydrogels with Rigid Hydrogel Mesh. (A) A soft collagen hydrogel mass is 3D printed alongside a sparse net of a more rigid alginate hydrogel. **(B)** Two steppers power a pair of syringe pump extruders with collagen and alginate hydrogel inks. **(C)** A hollow tube is printed from a soft hydrogel inside an alginate mesh to preserve its shape during handling or culture.

Most unmodified collagen hydrogel 3D prints cannot be lifted out of solution without introducing permanent deformation, and this is because the collagen hydrogel is too weak to support itself outside of solution. It was thought that including a rigid hydrogel such as alginate alongside the collagen would provide a reinforcement that would fuse to and sustain the collagen's geometry out of solution. A ring of printed collagen hydrogel supported by a printed alginate mesh shown in Figure 10A was shown to not only remained fused at the border of the two hydrogels but also maintain correct dimensions even after being transported in air multiple times. The largest dimensional deviation from the file was found at the sides of the alginate mesh, which were supposed to be 8 mm but turned out closer to 8.25 mm. The collagen ring was supposed to have an internal diameter of 4.4 mm and an outer diameter of 6 mm. In Figure 10B, the measurements for the edge of the alginate mesh, and the internal and external diameters of the collagen ring are shown. In another example, collagen sections which were manually plucked from their alginate mesh counterparts shown in Figure 10C brought with them portions of alginate mesh during dissection, as seen in Figure 10D. The fusion between the alginate and collagen portions of these multi-material prints is thought to be responsible for maintaining collagen geometry during handling. Furthermore, a multi-material collagen and alginate print of a scaled-up developing mammary duct survived a drop to the lab floor (Figure 10E). After it was recovered and imaged, it was shown to be intact and encased in alginate fibers clearly visible in Figure 10F. Further investigation into the maintenance of collagen geometry under handling forces is needed and will likely include material testing of multi-material prints. Since collagen by itself is a fragile material incapable of being delicately printed in a manner that bears its weight outside of solution, this method of reinforcing collagen with alginate presents a promising solution for creating and allowing the manipulation of complex collagen components. What's

more, the collagen can be isolated from the alginate without damage by submersion in a calcium chelating bath, which results in dissolution of the alginate mesh and complete release of the collagen component, as shown in Figure 10G. Due to the presence of the alginate mesh, it is noted that these constructs could be easily handled, seeded, cultured, and fixed without every touching or interfering with the collagen component.

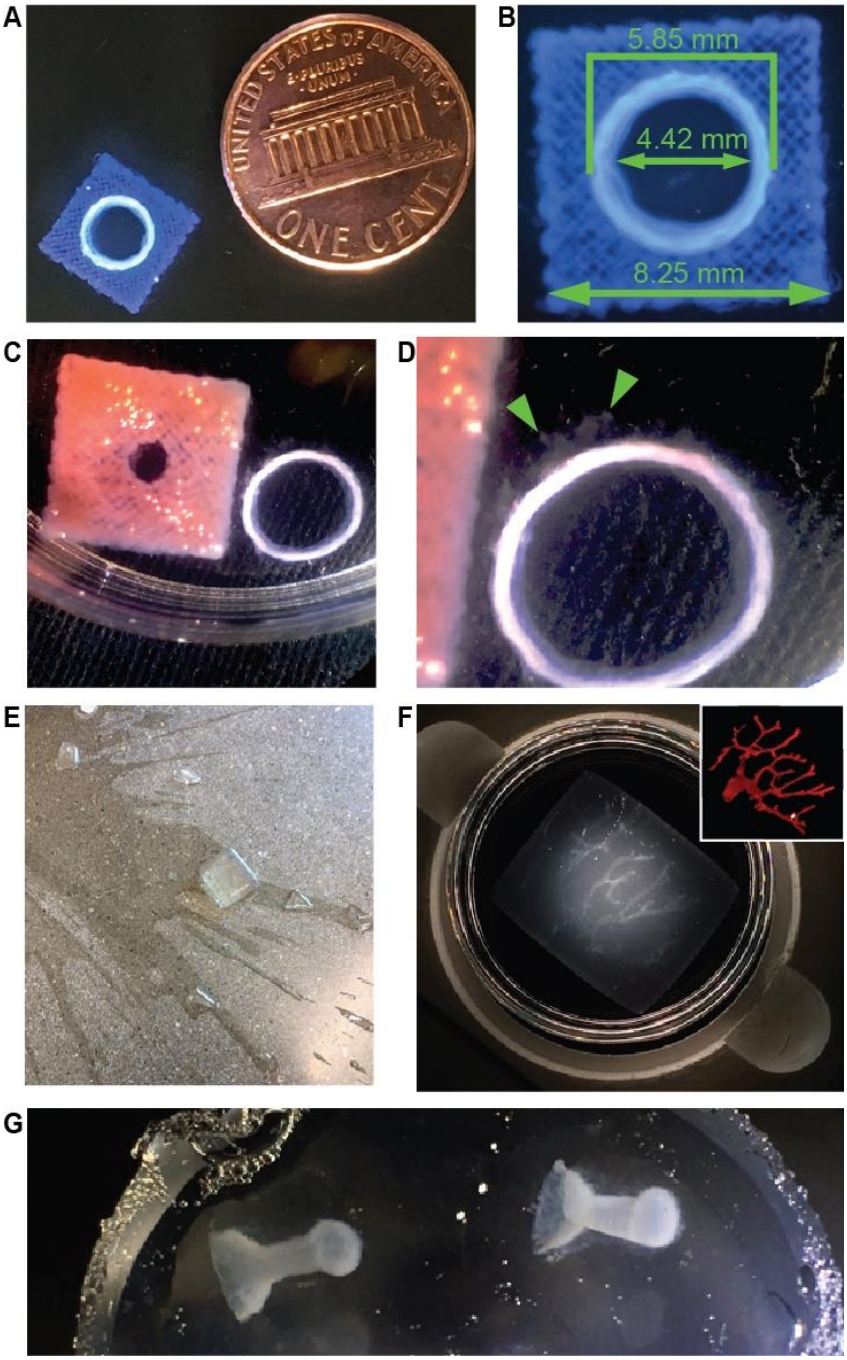

Figure 10. Stiff hydrogel components protect fragile hydrogel components in multi-material prints. (A) A multi-material print showing an inner ring of collagen hydrogel surrounded by alginate hydrogel stained with Alcian Blue. U.S. penny for scale. **(B)** The

measured construct shows dimensions consistent with the intended diameters. **(C)** A dissected multi-material print showing collagen ring on right and alginate mesh on left in pink **(D)** The removed collagen ring shows alginate fibers that were fused to the collagen and could not be separated, proving fusion of the gels. **(E)** A multi-material print is shown on the floor of a lab after having fallen several feet along with shards of its parent beaker. **(F)** The print in (E) recovered and under dark field illumination, showing maintenance of the fragile collagen component inside the print's interior. Inset is the file for the collagen component. **(G)** Collagen-based 3D printed tissues removed from alginate threads

Second, replicating the in vivo environment in vitro means engineering constructs to closely mimic the appearance of in vivo equivalents. The microscopic geometry of tissues is often more complex and dynamic than we can hope to recreate with any current technology, but macroscopic features are easily replicable using 3D printing. We can process imaging data (Figure 11A) from optical projection tomography (OPT) of whole-mount tissue samples, and, through software analysis, model the tissue as a 3D printable solid (Figure 11B). By printing an entire ductal epithelium modeled from imaging data, we can ensure that the internal features of the epithelium such as the bifurcations within the branching tree are geometrically representative of native tissues (Figure 11C). Furthermore, we can change our printed epithelium to a different model derived from a different set of imaging data or parametrically alter it to suit our needs.

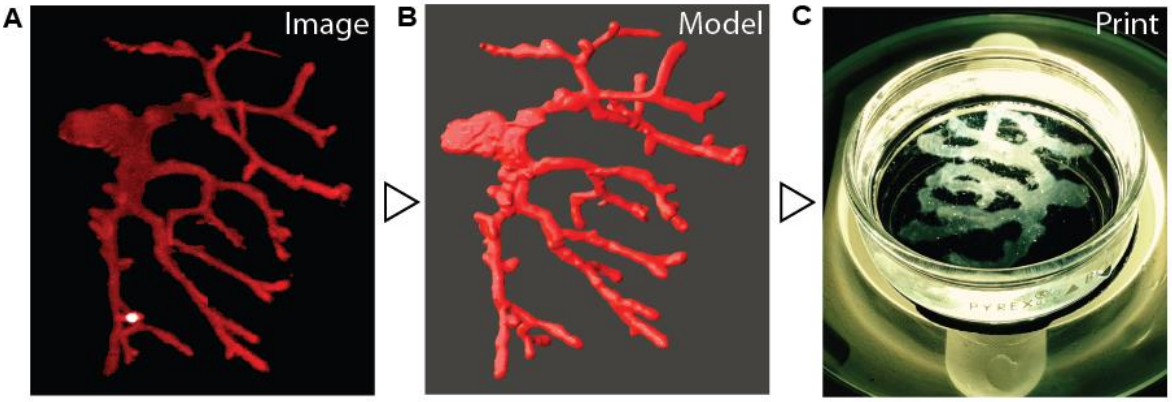

Figure 11. Imaging, modeling, and 3D printing a ductal epithelial tree. (A) A ductal epithelium tree is imaged using OPT or some other 3D scanning method. **(B)** A model of the ductal epithelium is generated from the imaging data. **(C)** A solid representation of the external geometry of the model is FRESH printed from a hydrogel shown in darkfield illumination.

Since it has been found that ductal epithelium possesses 4 distinct developmental morphologies, which are intimately associated with the 3 most commonly used mouse strains in breast cancer research, it is important to be able to vary the chosen geometry of the epithelium and obtain similar levels of accuracy across different morphologies. Verifying said accuracy of the 3D prints involves imaging them using a technique such as OPT or confocal microscopy, for the data obtained from such processes can be used to directly compare the output of the 3D printer with the input file's dimensions. We start by tackling conversion of complex image data stacks of epithelial tissues into 3D meshes that can be processed and 3D printed at numerous sizes and

shapes. Next, we draw from these structures a fundamental morphology and parametrically incorporate it into a representative parametric "module" designed in CAD. This module can be edited to account for any design shortcomings while still reflecting the necessary aspects of in vivo complexity.

Task 2 Subtask 2 consisted of tomography imaging and evaluation of 3D printed mammary ductal structure, with one sample to be evaluated. However, we are still working to further improve the imaging capability and to image the 3D printed mammary duct on the same OPT system used to collect the original whole mount image of the breast mammary duct from the mouse. We 3D printed a 200% scale ductal trees from collagen type I. The files used to generate these trees were obtained from Co-investigator Dr. Hadsell and processed through several iterations of workflow that eventually resulted in a continuous, manifold mesh without visible tiling artifacts, stacking artifacts, or floating solids shown below in Figure 12A. The file was scaled to 200% to allow the printer to deposit a significant portion of the construct using a filamentous extrusion shown in the Gcode in Figure 12B rather than as punctate depositions.

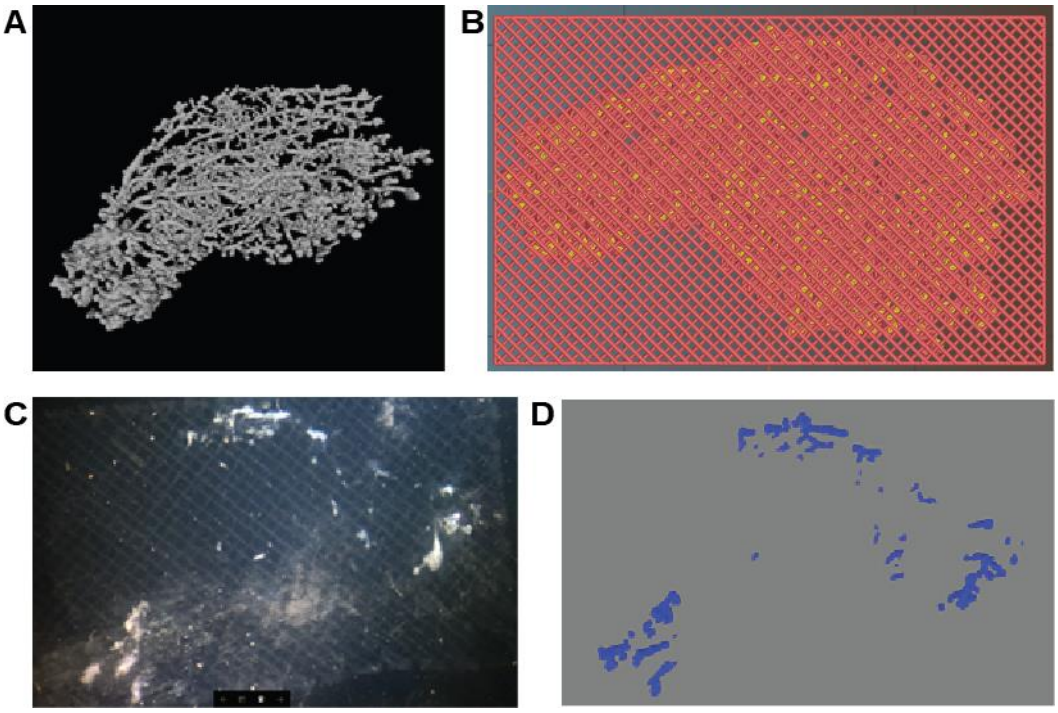

Figure 12. Producing Gcode for and troubleshooting a biomimetic mammary duct module. **(A)** A 6-wk. old KK/hlJ mammary duct is imaged and turned into this STL mesh representing the single largest connected surface which is, in turn, representative of the entire ductal tree. **(B)** Example Slic3r Gcode processing of (A), showing Collagen in yellow and alginate in red. **(C)** Printing the first 8 layers of the Gcode in (B) shows poor replication of collagen structures, which should appear like **(D)** The Gcode for the first 8 layers of collagen extrusion.

Executing the first few layers of the above Gcode using previously developed machine settings that worked best for simple constructs resulted in collagen extrusions shown in Figure 12C that

did not resemble the Gcode portion sent to the printer (Figure 12D). The poor quality of collagen extrusion shown in Figure 12C was attributed to subtle vibrations of the extruder tips along the Z axis during movement in the XY plane. These vibrations were thought to be caused by the formation and disappearance of moments on the extruder during faster movements. To account for this and other challenges presented by this print, it was decided to slow down the acceleration and instantaneous speed change settings to roughly half of their normal values. Additionally, the motors were provided with lower amounts of current to "smooth" out movements. Finally, the density of the alginate mesh support was increased from the 20% to 40%, providing much more support for collagen extrusions after release from the FRESH support bath.

Slower machine movements along with denser alginate mesh improved print quality substantially, resulting in the print shown in Figure 13A. This mammary duct model represents a world-first level of complexity generated using a bioprinter with multiple ECM and hydrogel components. This print takes approximately 2 hours to finish. Even at this slow rate, this print was printed faster than any commercial bioprinter could manage. A map of the printed construct generated using reflectance imaging tile scanning showed that features throughout the model were preserved in the output, shown below in Figure 13B and 13C. Distances measured between fiduciary regions of the file and print, shown highlighted with red stars in Figure 13B, indicated that the print underwent a roughly 4% shrinkage from its starting size. However, the shrinkage between fiduciary regions does not vary across at least one print. Repetition of these measurements are needed to confirm the maintenance of fidelity between file and print. Close-ups (Figure 13D) of the bottom left of the Gcode and the print's reflectance image in Figure 12 show that there is apparent visual fidelity between the Gcode and the print at areas of high detail. This 3D printed structure will serve as a starting point for fabricating a complete model of duct development and cancer *in vitro*. The walls of a construct such as this are thin enough (≤ 200 µm) that nutrient transport would not require vascularization. To fully utilize this model, many different support systems including perfusion culture and the endocrine effects of associated cell populations and stromal matrices would need to be incorporated. Even considering the challenges ahead, this model presents a complete solution to the mesoscale geometric complexity of branching epithelial networks.

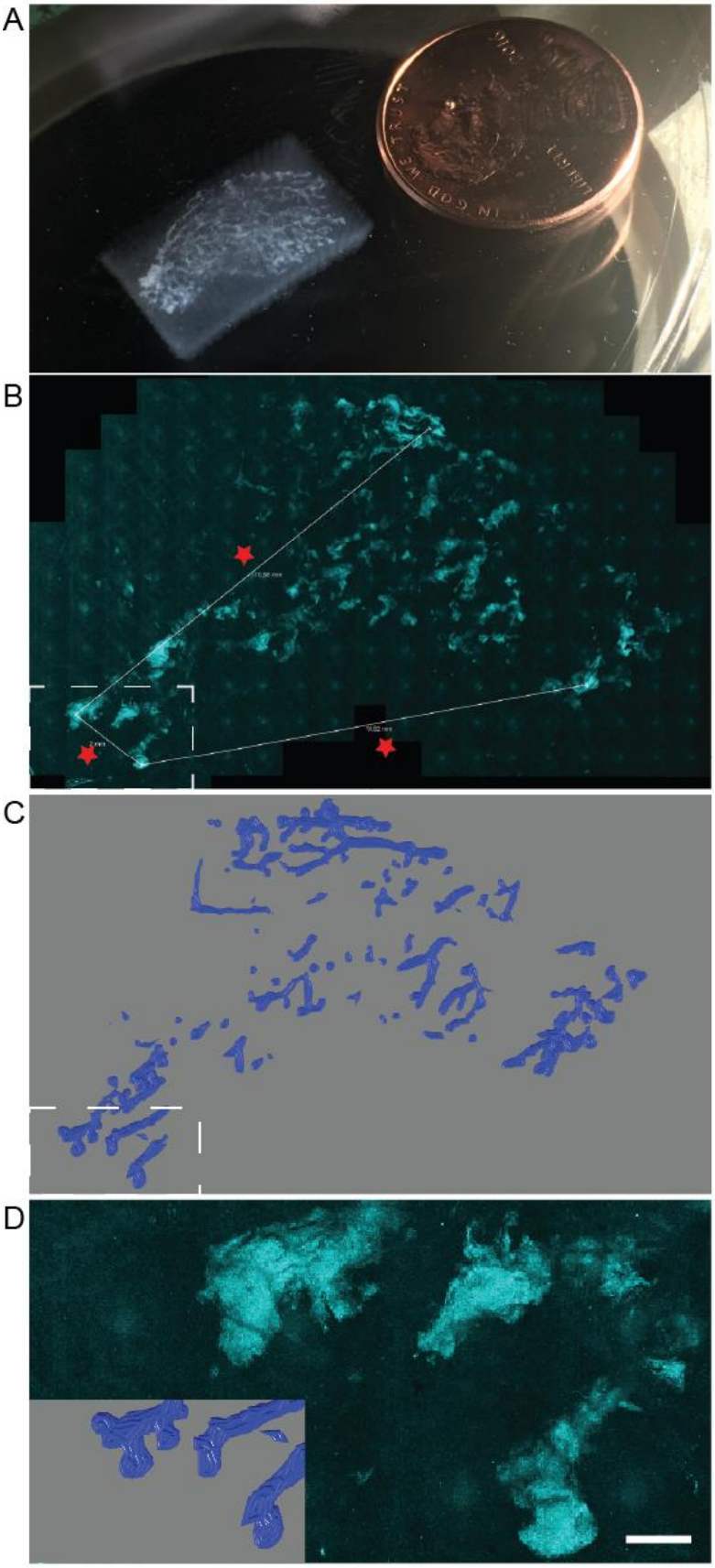
A
B
C
D

Figure 13. Biomimetic mammary duct print. (A) Shown submerged is the fully printed biomimetic collagen and alginate print of the file shown in Figure 4.8. The U.S. penny for scale shows that the print is faithful to the size of its file – 19 mm x 12 mm x 4 mm. **(B)** A max intensity projection of a reflectance tile scan shows that the print maintains fidelity in the first 12 layers of the print. The dashed box indicates an area shown in (D) Red stars indicate measured distances between fiduciary regions of the object. **(C)** Gcode of the first few layers of the print, showing the print maintains fidelity. Dashed box indicates area shown in **(D)** Close-up of the bottom left of (B & C) for comparison. Scale bar is 250 µm.

Task 2 Subtask 3 consisted of 3D printing the mammary ductal structure using progenitor cells (HMEC, MCF10A, HS578BSt). We have started this work and achieved the basic capability of seeding a simplified construct with mammary cells and evaluating adhesion, spreading and growth over time. Work is still ongoing to improve cell seeding and evaluate cell interaction.

To avoid the challenges of perfusion seeding and still enable distribution of cells throughout a construct with a sealed lumen, it was decided to try and seed constructs using a gravity-driven fluidic distribution system included in the mammary construct geometry. Mammary constructs had the same fundamental collagen component design of a funnel that fed into a tube "duct" which terminated in a spherical "bud". It was assumed that the funnel could be held up above the surface of cell culture media and used as a receptacle for a cell suspension and allow cell suspension to flow down into the rest of the construct through the walls of the duct and bud. It was hypothesized that, were it not possible to seed the sides of the duct and bud using this approach, then the construct could be seeded in waves, and the construct could be rested on its side to allow for each wave of cells in to coat the sides of the duct and bud. To allow for introduction of the cell suspension to the funnel and for resting of the construct on its side, the alginate mesh reinforcement was designed as a cube centered on and surrounding the collagen component.

Part of the design process for the mammary constructs revolved around the capabilities of the 3D printing software and the printer. Since the smallest diameter needles, we could utilize were 80 µm, we decided to design the collagen components to feature wall thicknesses in multiples of 80 µm. The interior lumen of the duct was the smallest feature of this print with an initial diameter of 200 µm in generation 1, but this value was increased to nearly 1 mm in generation 2. The resulting design features are shown in Figure 11. The size of the reinforcing alginate component was increased from 4 mm in X and Y to 8 mm to allow for easier handling of the entire construct.

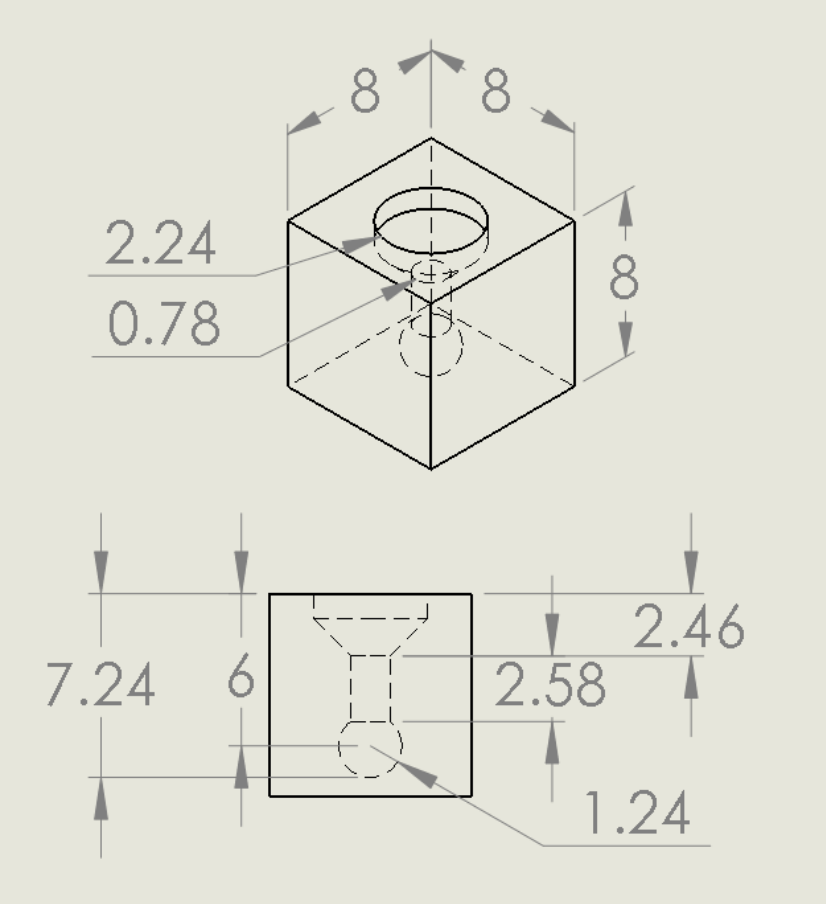

Figure 14. **The CONSTRUCT parametric mammary duct module.** The CONSTRUCT module features a vertical tube with a bulbous end and a funneled top. The dimensions of the construct were chosen based on what the printer was known to be capable of rendering in collagen type I.

For cell seeding post printing, constructs were thoroughly washed in warm 70 mM $CaCl_2$ with 25 mM Na-HEPES for at least 24 hours before submersion into 70 mM $CaCl_2$ with 25mM Na-HEPES and 50% v/v Ethanol. Constructs in this 50% Ethanol solution were then allowed to sit for 24 hours at 4°C. On the day of seeding and initiating culture, constructs were removed from this ethanol solution and placed into warm 70 mM $CaCl_2$ with 25mM Na-HEPES. After resting in this fluid for at least 30 minutes, the constructs were washed with fresh 70 mM $CaCl_2$ with 25mM Na-HEPES before being placed into cell media supplemented with 10 mM $CaCl_2$.

ATCC MCF7 (HTB-22) and ATCC MCF 10A (CRL-10317) cells were transfected with pHIV-ZSGreen lentivirus and flow sorted to select for transfected cells. Resulting cells were cultured per ATCC guidelines. Constructs were washed in sterile-filtered 20°C 1% $CaCl_2$ with 25 mM Na-HEPES. Constructs were then soaked in 20°C sterile-filtered ATCC media, supplemented with 10 mM $CaCl_2$ and 200 µg/mL Penicillin-Streptomycin for 10 minutes. Then constructs were placed in a 6-well plate with one construct per well. Supplemented media was added to each well until half of the construct was submerged (approximately 3 mL). Cells were suspended in supplemented media at 1 x 10^6 cells/mL. 50 µL of cells suspension was pipetted directly into the

center of the funnel portion of each construct. For half of the constructs, they were turned onto one of their 4 sides and allowed to rest there for 20 minutes at 37°C. Then, the seeding was repeated followed by 4 more resting periods until each construct was seeded on each side. Constructs were quickly imaged on an Olympus IX83 fluorescence microscope to ensure cells were in the constructs. One construct of the three for each cell type that was not rotated during seeding was seeded with 200,000 cells in the upright position. All constructs were finally returned to their upright conditions and placed in 37°C culture for 7 days, with regular media exchange. After 7 days, media was aspirated from each well before fixation.

Significant development effort was required to print these constructs. The most difficult aspect of this challenge was producing a wall of collagen material with uniform thickness across the entire length of the construct. After months of analysis, we determined that deflection of the small-diameter, 1 in long needle used as the extruder was the problem. During printing of the constructs for cell seeding, the needle was encountering the slurry's yield stress and was not able to exert a force large enough to overcome it until, like a spring, it developed a large enough internal strain – the deflection. Without physically altering the needle, it was thought that the Gcode instructions could be geometrically "hacked" to encourage the needle to more easily slide through the slurry. Typically, yield-stress fluids such as Bingham Plastics and Herschel-Bulkley models allow for the yield stress to dip if the fluid experiences a harmonic force. This effect is attributable to physical vibrations interfering with the bonds associated with the yield stress of the material. For the regions of the construct that were the most prone to needle deflection, it was though that a fine rectilinear raster pattern could be used to "jostle" the support and allow the needle to more easily progress. When this was applied to a couple of test prints, it was found to be unsuccessful in resolving closure of the duct. Therefore, it was necessary to physically reinforce the needle.

The 80 µm needle shown in Figure 15A was much stiffer after being reinforced (Figure 15B), and this allowed it to high-fidelity structures without closure of the duct (Figure 15C).

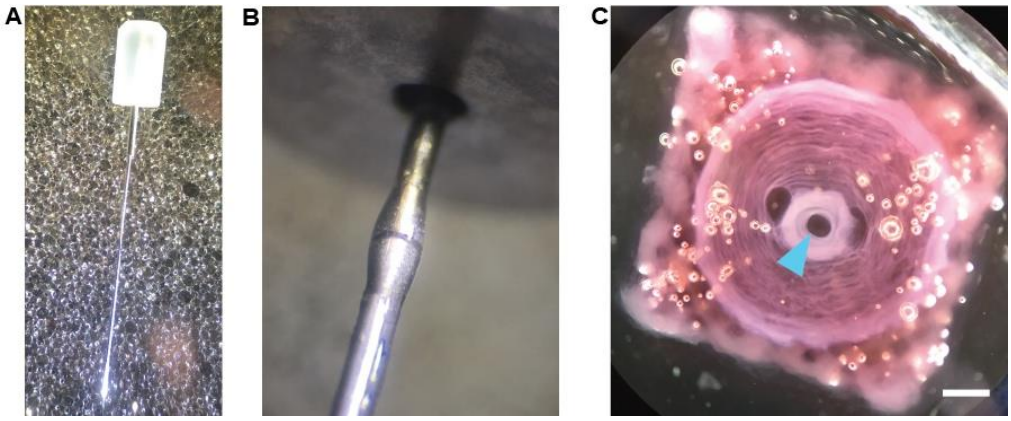

Figure 15. Physically reinforced needle produces better print outcome. (A) An un-reinforced 80 µm needle supplied by Hamilton for their GasTight® line of syringes with removable needle compression fittings. The glass ferrule is visible at the top, along with the slightly thicker section

of metal just below the ferrule. The bottom of this needle is very flexible compared to standard luer-lock disposable deposition tips available from a large variety of suppliers. **(B)** A 250 µm needle removed from a luer fitting is slid over the 80 µm needle until it contacts the thicker metal near the glass ferrule in (A) and epoxied in place. Epoxy is visible as a bulge of clear material near the seam of the 80 µm needle (top) and the length of 250 µm needle (bottom) **(C)** The resulting print performed with a reinforced 80 µm needle shows an open duct when looking from above, and the overall diameter of collagen paths is larger due the improved tracking of the 80 µm needle. Scale bar is 1 mm.

After the collagen extruder's needle was reinforced, constructs created in a coacervate slurry possessed perfectly concentric circular extrusions of collagen, with little to no deflection or lagging of the extrusion visible. This quality of output is largely attributable to both the extra-fine texture of the coacervate, which has monodisperse, microscopic particles and the attention paid to alignment of separate extruder needles pre-print. The exterior of the constructs possessed a square profile with the 90° crosshatch pattern of alginate mesh. The rim of the funnel nearly always possessed a diameter within 1% of the intended value. Initial data shows that the internal diameter of the duct falls within approximately 2% of its intended value. The same data indicates that when the prints were released, post-culture, they were found to possess buds that were always within 2% of the intended diameter of the file used to print them. Additional experimentation is still required to produce a statistically significant body of data.

Task 2 Subtask 4 involved tomography imaging and evaluation of 3D progenitor cell-printed mammary ductal structure. Following culture Cultured CONSTRUCT's were rinsed with 1X PBS (supplemented with 0.625 mM $MgCl_2$ and 10 mM $CaCl_2$) at 37°C, fixed in 4% w/v formaldehyde with 10 mM $CaCl_2$ (Polysciences, Inc.) for 15 min, and then washed 3 times in 11 mM $CaCl_2$ with 25 mM Na-HEPES. The fixed CONSTRUCT was imaged with a Nikon AZ-C2 macro confocal microscope with a 5x objective (0.45 NA) and a Leica SP5 multiphoton microscope with a 10x (NA = 0.4) objective and a 25x (NA=0.95) water immersion objective. 3D image stacks were deconvolved with AutoQuant X3 and processed with Imaris 7.5.

In cases where the collagen and cells were obscured by alginate threads, it was possible to remove the alginate by washing a fixed construct in a 100 mM Na-Citrate buffer solution for 12 hours. Then, the construct could be embedded in 10% w/v Gelatin A and sectioned. The resulting collagen component with attached interior cells was then accessible by the microscopes. After removal of alginate threads, we acquired 3D z-stacks using reflectance imaging of collagen I at 435 nm with a Leica SP5 multiphoton microscope and a 25x water objective (NA = 0.95). Using ImageJ, we measured the thickness of the collagen I hydrogels in cross-section.

It wasn't known if the method of gravity seeding the constructs would result in the formation of a monolayer of cells on the inside surface of the collagen component. Fluorescent images of cells seeded into the constructs showed that cells did not always reach the duct and the end bud. It is thought that, occasionally, gelatin solution from the melting of the FRESH support bath does not entirely clear the duct and bud during post processing. In cases where gelatin may remain in the throat of the duct, it could prevent cell solution from entering the construct due to its viscosity. This blockage of cell suspension results in the seeded cells populating only the top portion of the

duct and the funnel, as shown in Figure 16A. MCF7 cells expressing GFP are shown completely covering the surface of the funnel in Figure 16B.

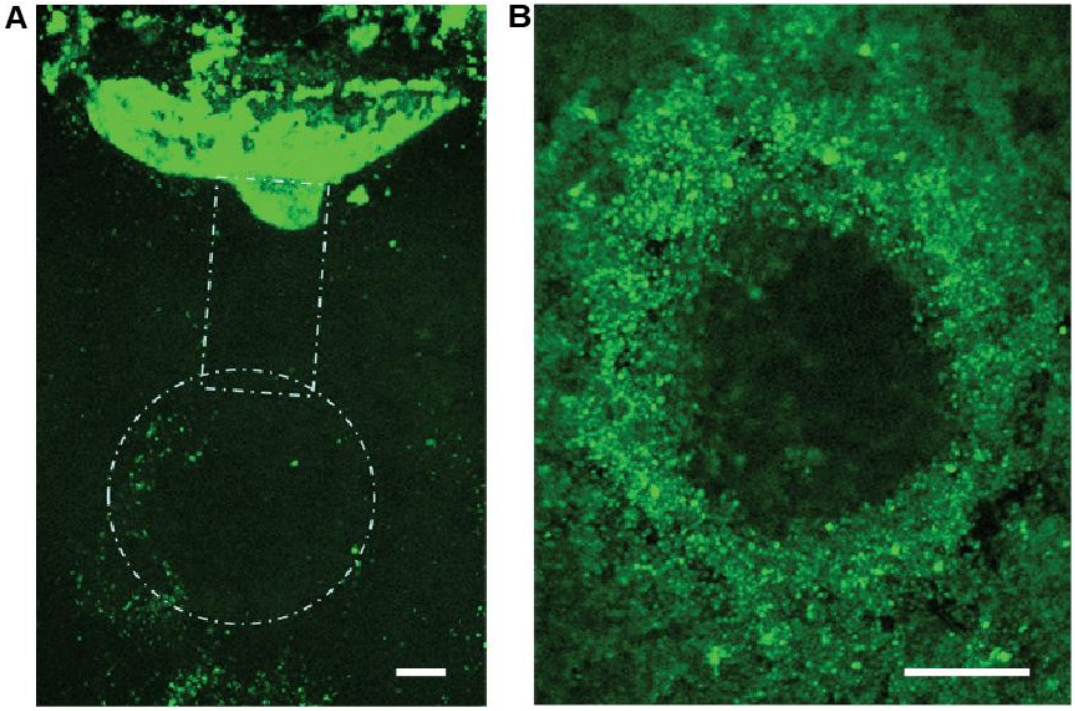

Figure 16. Seeding constructs can fail if the central tube of the construct is blocked with molten gelatin. (A) After a week of culture, MCF7 cells expressing GFP are shown to crowd the entrance to the CONSTRUCT, the rest of which is shown outlined in white dotted lines. It is thought that the cell suspension used to seed this construct could not enter the central tube and the terminal bud due to gelatin or excess hydrogel blocking the central tube. **(B)** A view from the top of the construct showing MCF7 cells adhered and growing in clusters around the entrance to the central tube. Scale bars are 1 mm.

In constructs seeded with MCF7 cells, fluorescence of cells was punctate and indicative of cells not covering the entire collagen surface inside the construct. Instead, cells grew in clusters, and the population of cells lining the duct and mouth of the funnel appeared rough, not possessing a smooth luminal surface, as seen in Figure 16B. In cultures of MCF10A cells, cell spreading on the constructs was much more pronounced, and cells formed a much smoother lumen shown in Figure 17.

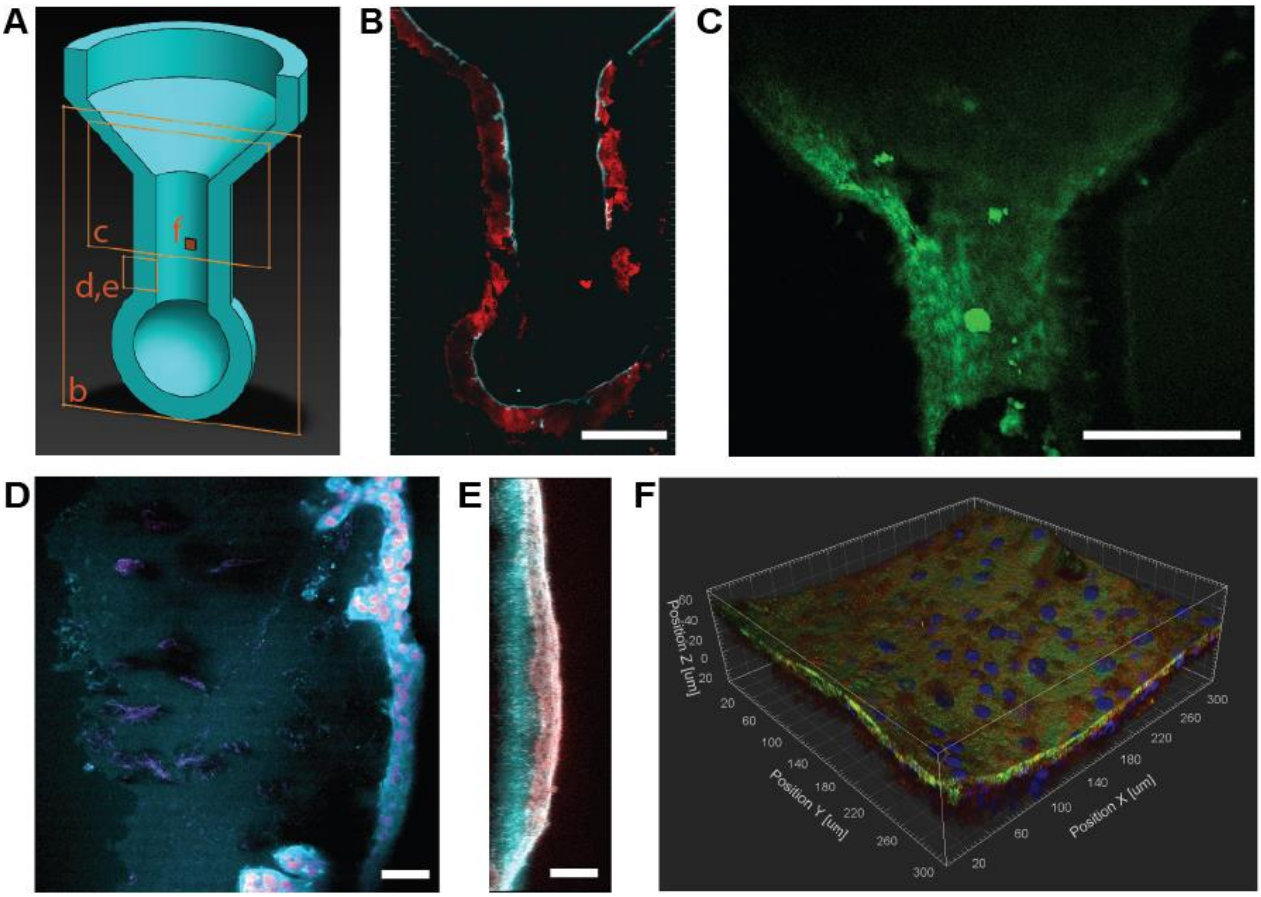

Figure 17. An epithelium of MCF10a cells coats the interior surface of a construct. (A) The CONSTRUCT shown with a cutaway to illustrate the regions imaged and shown in (B-F) **(B)** Collagen reflectance shown in red and GFP expression of MCF10a cells shown in cyan demonstrates the presence of a thin, continuous epithelium situated at the inside border of printed collagen hydrogel. **(C)** A max intensity projection of the construct shown in (A) which displays a coating of GFP-expressing MCF10A cells on the internal surface of the collagen. For (A) and (B) Scale bars are 1 mm. **(D)** Cyan actin (phalloidin) fluorescence with nuclei (DAPI) shown in magenta. The epithelium shows evidence of invading the collagen layers, as is shown by appendages of the epithelium extending from the luminal side (right) into the collagen. The exterior border of collagen is visible on the left of the image as a slight cyan fluorescence coming from overlap of the eosin fluorescence with actin fluorescence. Scale bar is 100 µm. **(E)** Another view of the epithelium showing cyan protein stain (eosin) and magenta actin (phalloidin) fluorescence with a clear boundary between cells and underlying collagen. Scale bar is 100 µm. **(F)** An isometric view of a z-stack of CONSTRUCT epithelium showing green actin (phalloidin), blue nuclei (DAPI), and red protein (eosin) fluorescence.

The number of cells required to get adequate coverage of the collagen surfaces inside the construct was quite substantial – 50,000 cells per construct. MCF10A's expressing GFP were visibly covering the interior of the duct and bud, shown in Figure 17B and 17C. Gravity seeding constructs did not result in cells lining the top side of the bud, which is to be expected since settling cells will not have access to this portion of the construct. Interestingly, however, cells

populated every other interior surface including the vertical walls of the duct tube. During culture, it may have been possible for cells to spread through defects to the outer surface, but no significant fluorescence was seen on collagen component exteriors. However, it is evident in Figure 17D that MCF10A cells are invading the collagen wall and are capable of smoothing the chaotic surface of the collagen which is slightly visible as a fuzzy cyan border on the left side of the image. In Figure 17E, the border between cells and collagen is clearly visible, but this was not the case for the entire construct. A representative picture of epithelium on the interior surface, shown in Figure 17F, indicates that the cells form a smooth, multi-layered surface of cells regardless of the underlying collagen. Many iterations of seeding and construct design/print process were utilized to arrive at the current results. It is believed that the current seeding method will only benefit from higher cell numbers, and future plans include many replicates for the sake of obtaining statistically powerful insights on the nature of these rapidly prototyped tissues.

One concern regarding these constructs was whether the cells would compact the collagen component and cause a loss of structure. In all cases, constructs showed some degree of delamination between the alginate and collagen sections of the constructs visible at the rim of the funnel (Figure 18), regardless of cell type used. It is thought that this disconnection was the result of the collagen-alginate connection being particularly weak at the rim of the funnel. In future iterations of the construct, it would be straightforward to completely embed the rim of the construct into the surrounding alginate mesh fibers, thereby preventing it from disconnecting. To investigate the effects of cells on the interior dimensions of the collagen component, it will be necessary to repeat these experiments and utilize a tomographic imaging approach to resolve internal architecture.

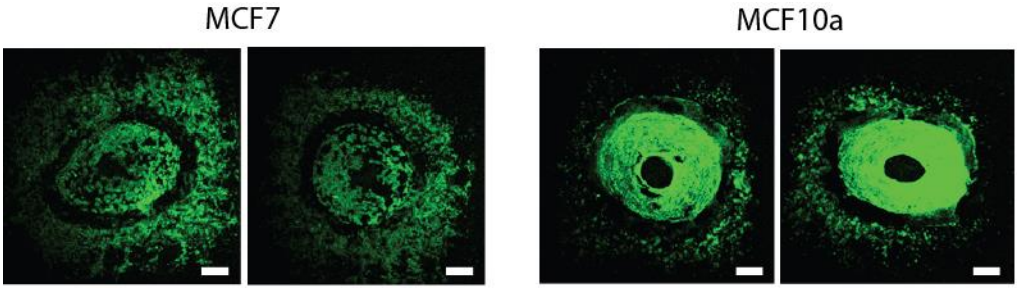

Figure 18. Delamination of collagen is consistent across constructs seeded and cultured for a week. Constructs shown on the left were cultured with MCF7 cells, and constructs on the left were cultured with MCF10a cells. In all constructs, a gap of cells was visible around the top rim of collagen, indicating that the collagen was originally there but pulled away under the action of cells. Otherwise, we would expect to see cells scattered around the edge of the rim on all regions of top-side alginate. Scale bars are 1 mm**.**

We successfully 3D printed a mammary duct in different configurations and imaged them in 3D using optical coherence tomography (OCT). As shown in Figure 19, we created different CAD model designs with a linear tube and 3D printed these our of collagen (Figure 19A and 19B). We then used OCT to verify fidelity of the printed structures. Cross-sections show that we achieved luminal diameters of ~1 mm and a wall thickness of ~300 μm (Figure 19C and 19D).

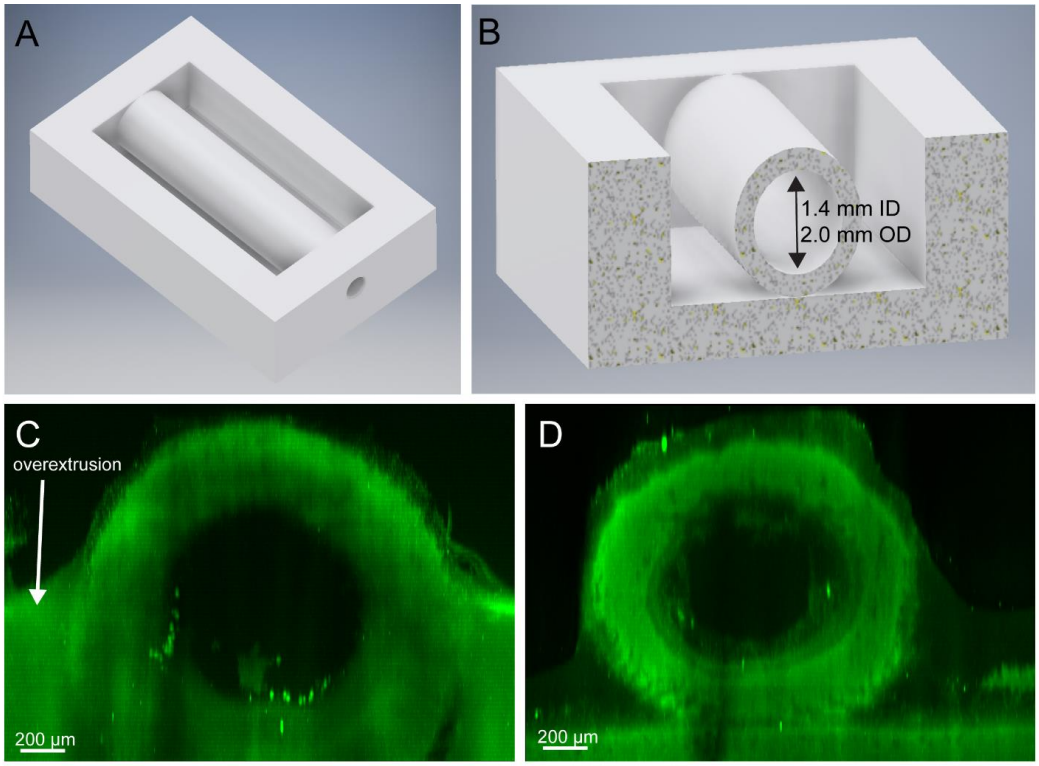

Figure 19. Printing Fidelity Improvement with New Syringe Pump: (A) A CAD model of a single duct **(B)** A cross-section of the duct demonstrating its inner and outer diameters **(C)** A duct 3D bioprinted using collagen type I on our previous generation hardware, demonstrating overextrusion of material leading to decreased print fidelity **(D)** A duct 3D bioprinted using our new syringe pump, showing greater fidelity when compared to the CAD model.

Task 2 Subtask 5 involved 3D printing a mammary gland using both luminal and myoepithelial cells. We were able to success 3D print a mammary gland construct using collagen type I and then post seeding using luminal and myoepithelial cells. Detailed analysis of the structure and cellularization of this construct is described in the results of the imaging for Subtask 6.

Task 2 Subtask 6 involved tomography imaging and evaluation of 3D luminal and/or myoepithelial cell-printed mammary glands. Previously we seeded MCF7 cells onto 3D bioprinted discs of collagen type I. In these samples we saw the successful formation of a monolayer and subsequent degradation of the sample by the MCF7 cells. When human primary breast duct epithelial cells were seeded on collagen type I discs, we also saw the successful formation of a monolayer (Fig 17). At the edges of the disc we saw spontaneous formation of a bilayer, with one layer staining positively for an epithelial marker (cytokeratin K8) and the other staining positively for a myoepithelial marker (cytokeratin K5) suggesting that the 3D bioprinted collagen scaffold provided a sufficient environment to recapitulate bilayer formation found in the epithelium of breast ducts.

Due to the spontaneous bilayer formation of primary breast cells seeded onto 3D bioprinted collagen scaffolds, we choose to engineer more anatomically relevant tubular collagen

constructs. Initially we used a 1.4 mm inner diameter tube with a 300 μm wall, thin enough to allow for diffusion of oxygen and nutrients to support any cells growing on the inner surface of the tube (Figure 20A). We next seeded human primary breast duct epithelial cells at 10 million cells/mL into the duct through its open ends using a syringe. These cell laden constructs were then cultured for 14 days, fixed, and stained for cytokeratin K8 (red) to identify the epithelial cells and K5 (green) to identify myoepithelial cells (Figure 20B). These initial samples looked promising, with good formation of an epithelial/myoepithelial bilayer covering the inner lumen of the tubular prints. In Figure 20B we can see a top-down maximum intensity projection of one of these tubular constructs with several cross sections called out in end-on maximum intensity projections. In Figure 20C we see a zoomed in top down view of the walls, showing the bilayer.

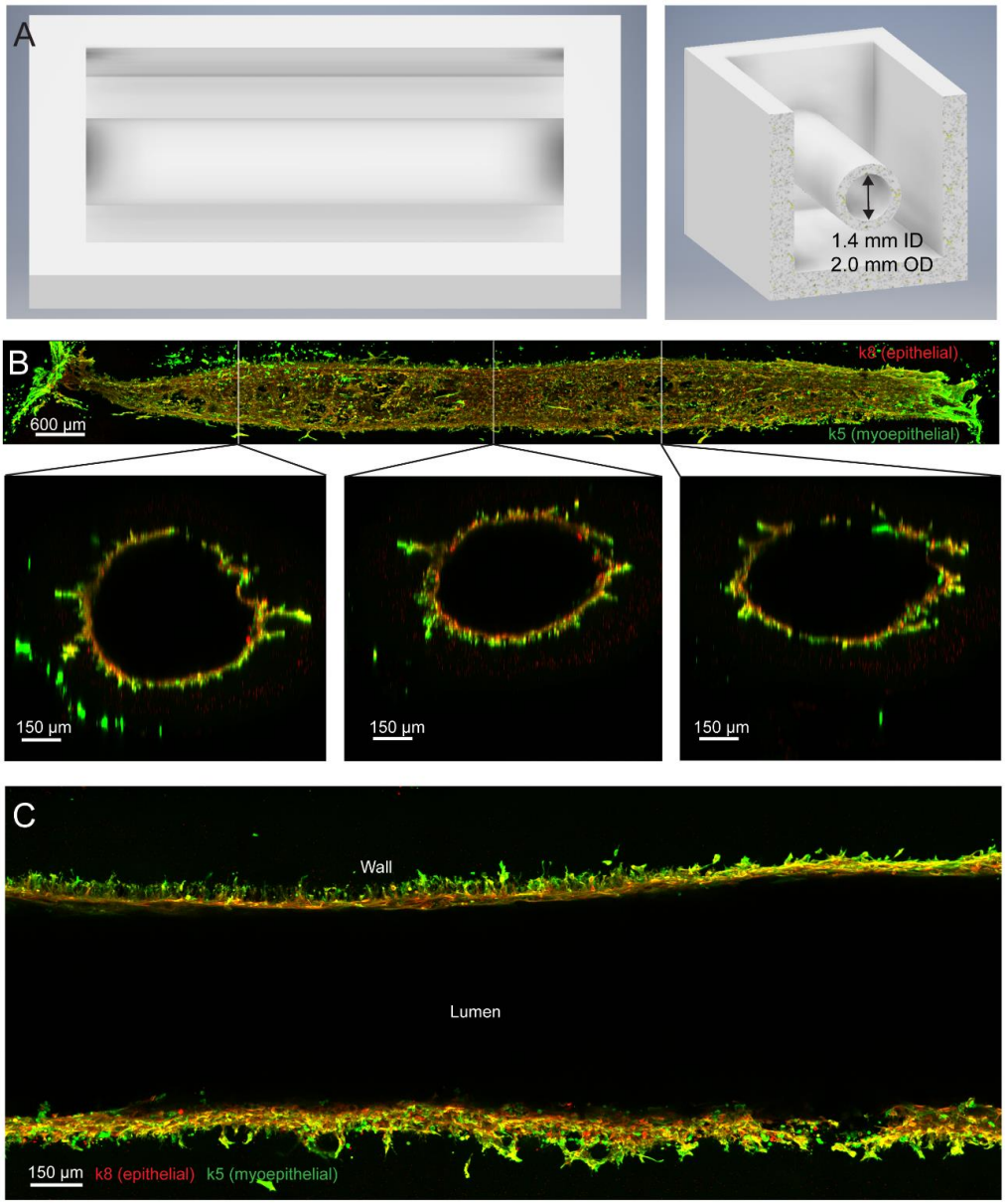

Figure 20. Fluorescence Imaging of an Epithelialized Collagen I Tube: (A) CAD model of a ductal tube with an inner diameter of 1.4 mm and a wall thickness of 300 microns **(B)** Top-down maximum intensity projection of the full length of a tube with cytokeratin k8, a marker of epithelial cells, in red and cytokeratin k5, a marker of myoepithelial cells, in green. Three cross-sections are called out demonstrating the spontaneously formed epithelial/myoepithelial bilayer. **(C)** A Top-down maximum intensity projection taken from the center of the tube, showing the lumen and the walls as well as the epithelial/myoepithelial bilayer.

Task 3 subtask 1 involved injecting cells into printed mammary ducts and monitoring growth and progression. Initial results placing cells in the 3D printed mammary scaffold were not conducive to growth and measurement. We therefore redesigned the printed construct and the bioreactor platform to support growth and culture of the construct. We redesigned the platform

and included a bioreactor system that would enable controlled fluid flow for cell seeding coupled with controlled fluid flow throughout the culture process to ensure proper nutrient supply and waste removal.

In Figure 21 we show the redesigned mammary duct tube designed and constructed in Year 2. This system is printed entirely in collagen type I and has an inner diameter of 1.4 mm, to match a nominal size in the human breast (Figure 21A). We have achieved highly repeatable 3D printing using our FRESH technique and have produced >50 of these constructs with no issues and extremely high fidelity (Figure 21B and 21C). We have validated that the tube that serves as the mammary duct is manifold and performed perfusion studies that have shown low permeability using various molecular weight dextran solutions, to simulate biological molecules.

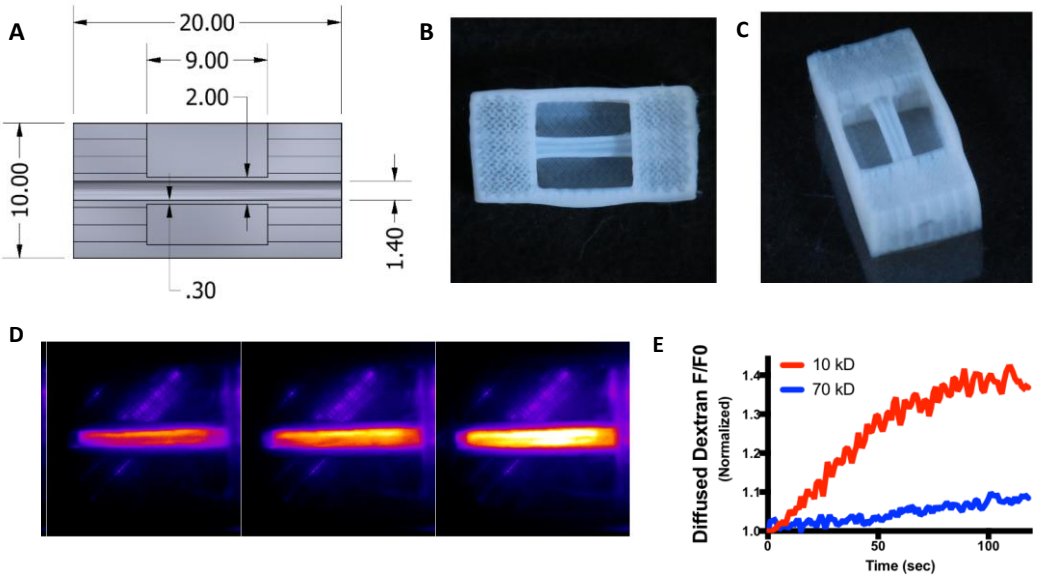

Figure 21. The redesigned mammary duct construct showing the simplified tube design and perfusion validation. (A) Schematic of the construct. (B and C) Photographs of the construct printed entirely from collagen type I using the FRESH 3D bioprinting method. (D) Perfusion studies using our bioreactor platform to perfuse fluorescent Dextran of various molecular weights through the lumen and tracking diffusion through the tube wall. (E) Quantification of the perfusion and permeability studies in (D), showing as expected that diffusion through the wall depends on molecular weight, but also that there are no large defects.

In Figure 22 we show that this redesigned mammary construct also enables straightforward engineering of stromal tissue around the mammary duct tube by casting a collagen gel with embedded cells. The previous duct and end bud construct developed in Task 2 in year 1 enabled luminal seeding, but the surrounding alginate support prevent creation of stromal-like tissue. Here the empty region around the tube can be filled with a collagen gel with embedded stromal cells (Figure 22A). We then culture this as normal and show that the stromal tissue around the tube can contain viable cells (Figure 22B).

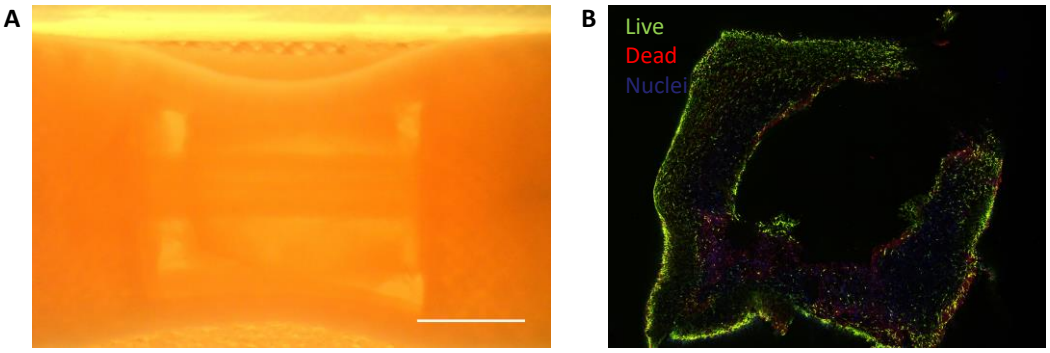

Figure 22. Example of the redesigned mammary construct with the addition of stromal-like tissue around the ductal tube in the center of the construct. (A) A brightfield image of the construct inside the bioreactor perfusion system with a collagen gel with embedded cells cast around the central tube region. (B) A cross-section of the tube construct that has been sectioned and stained with LIVE/DEAD showing uniform cell distribution throughout shortly after fabricating the entire construct.

We also developed improved 3D bioprinting hardware in order to be able to 3D print mammary gland scaffolds that are closer in size to smaller ducts in the human breast. With this new hardware we began to print tubes with single inner diameters and tapered entrance ports to allow for insertion of a micropipette tip. These were printed in 400 µm inner diameter and 200 µm inner diameter versions (Figure 26A and 26B respectively). We also confirmed the patency of the lumens of these constructs using optical coherence tomography (Figure 26C and 26D).

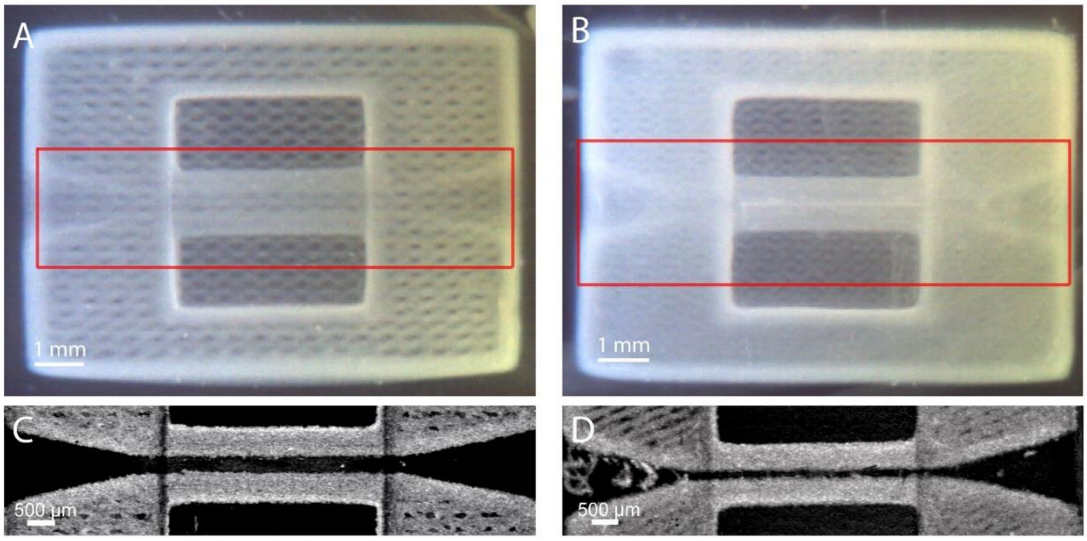

Figure 23. Working Towards Anatomically Accurate Ductal Inner Diameters: (A) Top-down image of a ductal print in collagen type I with an inner diameter of 400 microns **(B)** Top-down image of a ductal print in collagen type I with an inner diameter of 200 microns **(C)** Optical coherence tomography of the print in (A) demonstrating a patent inner lumen **(D)** Optical coherence tomography of the print in (B) demonstrating a patent inner lumen

Task 3 Subtask 2 was to stain and collect tomography image data for 3D ductal structures injected with premalignant breast cells. For cell seeding we printed tubes with a change in the lumen diameter along its length from 1.4 mm to 600 µm (Fig. 24A). These were successfully seeded using a micropipette, without penetrating the lumen wall (Fig. 24B). In Figure 24C a maximum intensity projection of a seeded tube after 14 days of culture can be seen, again demonstrating epithelial and myoepithelial layers. The scarcity of cells in the smaller diameter lumen section suggests that we need to increase the cell density of our seeding solution. We can also begin to directly print very high concentration cell inks to ensure that sufficient numbers of cells are placed within the tube lumens.

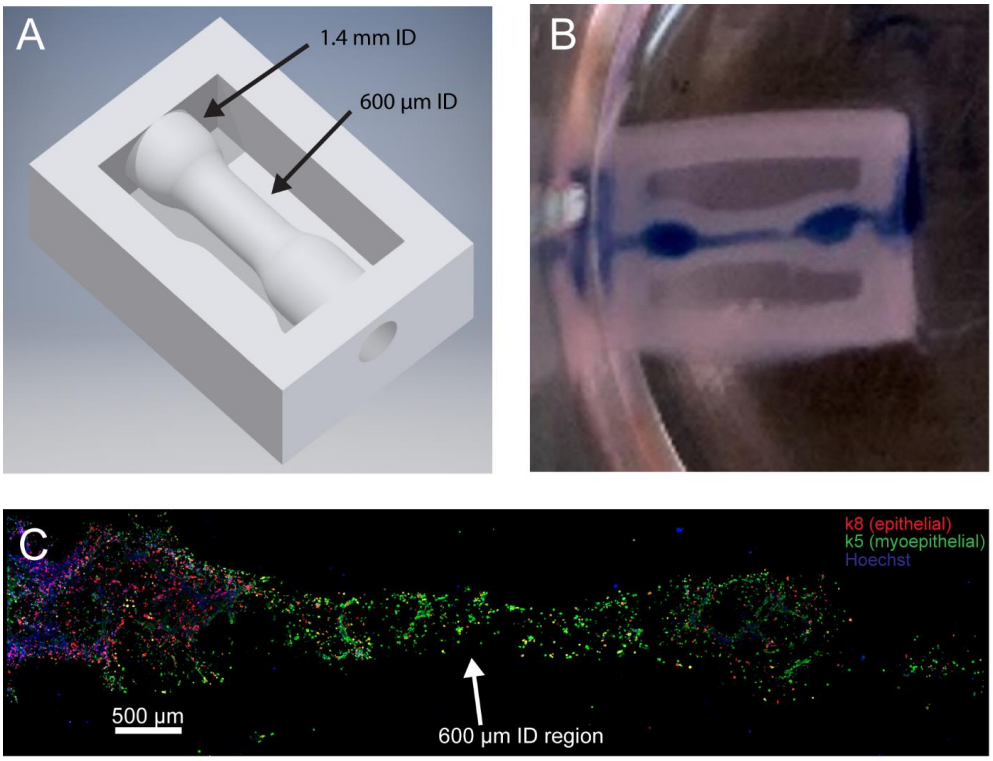

Figure 24. Seeding Smaller Inner Diameter Ductal Prints: (A) CAD model with a stepped change in inner diameter from 1.4 mm to 600 microns **(B)** Top-down image of a ductal print in collagen type I after seeding with primary breast epithelial cells (Trypan blue used for contrast) **(C)** Fluorescence imaging of the seeded construct with a nuclear stain in blue, cytokeratin k8, a marker of epithelial cells, in red and cytokeratin k5, a marker of myoepithelial cells, in green.

Task 3 Subtask 3 involved comparing reconstructions among and within 3D ductal structures to detect variations in pattering and invasive behavior. In addition to single tube constructs shown in results for previous subtasks, advancements in our FRESH 3D bioprinting platform have allowed us to begin to develop simple networks that incorporate ducts as well as end buds to recapitulate some of the aspects of mammary networks found *in vivo*. In Figure 25A we can see a CAD model of such a network, which has lumen inner diameters of 2 mm and end bud diameters of 3.2 mm. In Figure 25B we can see this network printed in collagen type I and in Figure 25C we can see that these lumens are patent, as they allow for perfusion of a dye.

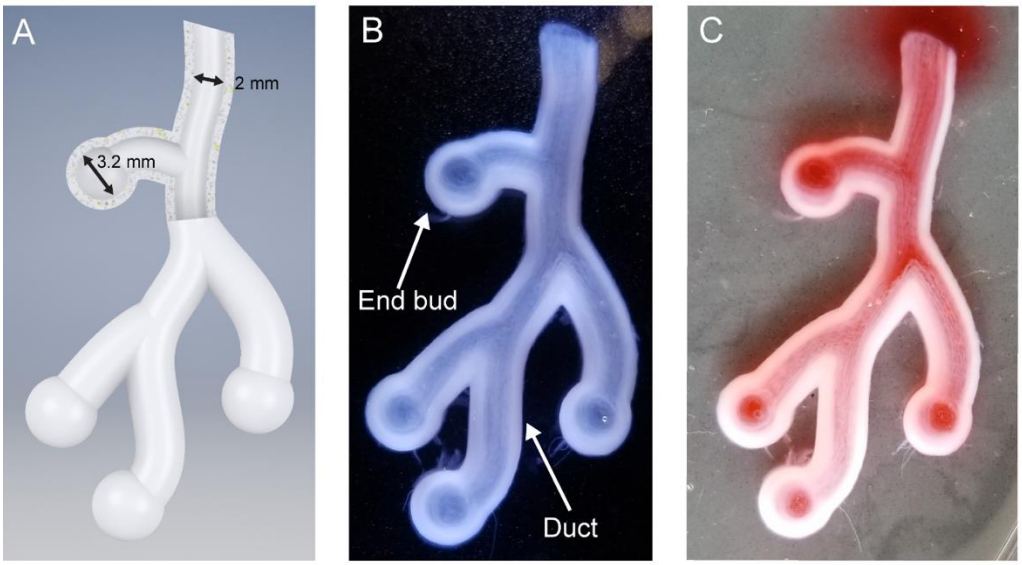

Figure 25. More Complex Breast Duct Networks: (A) Intermediate complexity CAD model with multiple ducts and end buds. **(B)** Top-down image of a ductal print in collagen type I **(C)** Top-down image of the ductal print after perfusion with dye, demonstrating patency of the lumen.

Task 3 Subtask 4 involved writing the manuscript "3D Bioprinting a human model of DCIS". This manuscript has been drafted, but it is not yet submitted. Submission is planned for early 2020.

Task 4 focused on RNA-seq analysis of premalignant progression. This task was not started because of the challenges encountered during Task 3 to engineer a model of the mammary duct that provided acceptable ability to achieve and monitor growth.

Task 5 focused on Functional screen for genes important in progression and experimental**.** This task was not started because we were waiting for results from Task 4.

4) Impact

Our data indicate that different strains of mice exhibit different mammary gland structures, suggesting a genetic component to development. This ties in with data showing genetic differences in susceptibility to mammary tumorigenesis and metastasis. Having a comprehensive quantification of mammary gland development may yield insight into risk factors for subsequent development of breast cancer. This work is close to finished and will be submitted for publication. We expect this work to be of great interest to those in the field of mammary gland biology and breast cancer.

We achieved the primary goal of 3D printing a model of the mammary gland and ductal network. This has required major advances in 3D bioprinting hardware that we have designed and improvements in the 3D bioprinting of collagen type I bioinks. In fact, the advances we made were cutting edge, and the results were published in part in *Science* in August 2019 and were supported in part by this research funding. We have also drafted a manuscript on the 3D

bioprinted mammary duct as described in the results and plan to submit this for publication in January 2020.

The results we have generated and either published or plan to publish soon provide a strong scientific foundation for further study. Though we did not fully achieve our vision of an *in vitro* model of DCIS, we took critical steps towards it. We plan to submit an R01 proposal to the National Cancer Institute at NIH for follow on funding in late 2020 once our manuscript to be submitted early 2020 is published.

5) Changes/problems

We encountered minor difficulties such as reduced fecundity in some mouse strains, but we continued these studies and complete the mammary ductal development studies as noted above. We encountered major challenges in the design and implementation of the 3D ductal microenvironment, as the method we initially developed showed uneven plating of cells and delamination of collagen. We re-engineered the 3D ductal environment to allow perfusion and easier plating of cells. This redesign tackled several new areas of 3D bioprinting.

6) Products
Whole mounts of murine mammary glands
Images and reconstructions of mammary glands
3D printed tubes with perfusion representing ducts

Oral Presentations:
"Engineering an in vitro Model of Ductal Carcinoma In Situ Using FRESH 3D Bioprinting," J. Tashman, T. Hinton, D. Brown, D. Shiwarski, A. Lee, A. Hudson, A. Lee, A. Feinberg, Society for Biomaterials 2019 Annual Meeting, April 3, 2019, Seattle, WA.

Publication:
A. Lee, A. R. Hudson, D. J. Shiwarski, J. W. Tashman, T. J. Hinton, S. Yerneni, J. M. Bliley, P. G. Campbell, and A. W. Feinberg, "3D Bioprinting of Collagen to Rebuild Components of the Human Heart," ***Science***, Vol. 365, Issue 6452, 2019, pp. 482-487.

7) Participants and other collaborating organizations
Adrian V. Lee, PhD, University of Pittsburgh (PI)
Adam Feinberg, Carnegie Mellon University (partnering PI)
Darryl Hadsell PhD, Baylor College of Medicine (subcontract to PI)
Priscilla McAuliffe MD, PhD University of Pittsburgh (Co-Investigator)

8) Special reporting requirements
None

9) Appendices
None